



HAL
open science

Inversion of CO and NO_x emissions using the adjoint of the IMAGES model

J.-F. Müller, T. Stavrakou

► **To cite this version:**

J.-F. Müller, T. Stavrakou. Inversion of CO and NO_x emissions using the adjoint of the IMAGES model. Atmospheric Chemistry and Physics, 2005, 5 (5), pp.1157-1186. hal-00295653

HAL Id: hal-00295653

<https://hal.science/hal-00295653>

Submitted on 18 Jun 2008

HAL is a multi-disciplinary open access archive for the deposit and dissemination of scientific research documents, whether they are published or not. The documents may come from teaching and research institutions in France or abroad, or from public or private research centers.

L'archive ouverte pluridisciplinaire **HAL**, est destinée au dépôt et à la diffusion de documents scientifiques de niveau recherche, publiés ou non, émanant des établissements d'enseignement et de recherche français ou étrangers, des laboratoires publics ou privés.

Inversion of CO and NO_x emissions using the adjoint of the IMAGES model

J.-F. Müller and T. Stavrakou

Belgian Institute for Space Aeronomy, Brussels, Belgium

Received: 5 October 2004 – Published in Atmos. Chem. Phys. Discuss.: 6 December 2004

Revised: 22 February 2005 – Accepted: 23 March 2005 – Published: 25 May 2005

Abstract. We use ground-based observations of CO mixing ratios and vertical column abundances together with tropospheric NO₂ columns from the GOME satellite instrument as constraints for improving the global annual emission estimates of CO and NO_x for the year 1997. The agreement between concentrations calculated by the global 3-dimensional CTM IMAGES and the observations is optimized using the adjoint modelling technique, which allows to invert for CO and NO_x fluxes simultaneously, taking their chemical interactions into account. Our analysis quantifies a total of 39 flux parameters, comprising anthropogenic and biomass burning sources over large continental regions, soil and lightning emissions of NO_x, biogenic emissions of CO and non-methane hydrocarbons, as well as the deposition velocities of both CO and NO_x. Comparison between observed, prior and optimized CO mixing ratios at NOAA/CMDL sites shows that the inversion performs well at the northern mid- and high latitudes, and that it is less efficient in the Southern Hemisphere, as expected due to the scarcity of measurements over this part of the globe. The inversion, moreover, brings the model much closer to the measured NO₂ columns over all regions. Sensitivity tests show that anthropogenic sources exhibit weak sensitivity to changes of the a priori errors associated to the bottom-up inventory, whereas biomass burning sources are subject to a strong variability. Our best estimate for the 1997 global top-down CO source amounts to 2760 Tg CO. Anthropogenic emissions increase by 28%, in agreement with previous inverse modelling studies, suggesting that the present bottom-up inventories underestimate the anthropogenic CO emissions in the Northern Hemisphere. The magnitude of the optimized NO_x global source decreases by 14% with respect to the prior, and amounts to 42.1 Tg N, out of which 22.8 Tg N are due to anthropogenic sources. The NO_x emissions increase over Tropical regions, whereas

they decrease over Europe and Asia. Our inversion results have been evaluated against independent observations from aircraft campaigns. This comparison shows that the optimization of CO emissions constrained by both CO and NO₂ observations leads to a better agreement between modelled and observed values, especially in the Tropics and the Southern Hemisphere, compared to the case where only CO observations are used. A posteriori estimation of errors on the control parameters shows that a significant error reduction is achieved for the majority of the anthropogenic source parameters, whereas biomass burning emissions are still subject to large errors after optimization. Nonetheless, the constraints provided by the GOME measurements allow to reduce the uncertainties on savanna burning emissions of both CO and NO_x, suggesting thus that the incorporation of these data in the inversion yields more robust results for carbon monoxide.

1 Introduction

The emissions of the ozone precursors carbon monoxide (CO), nitrogen oxides (NO_x) and non-methane volatile organic compounds (NMVOCs) have a profound influence on both tropospheric ozone, a key actor in air quality and climate change, and the hydroxyl radical (OH), the primary oxidizing agent and scavenger of many gases, including methane and the other ozone precursors.

In the “bottom-up” approach for estimating the emissions, geographical and statistical data are used to extrapolate measurements of emission factors, typically available only on a sparse spatial and temporal network. This extrapolation of local measurements generates important errors, due to the high spatio-temporal variability of emission fluxes. As a result, the current emission inventories are highly uncertain. In the “top-down” or inverse modelling approach, the surface emissions used in a chemistry-transport model (CTM) are adjusted in order to minimize the discrepancy between

Correspondence to: J.-F. Müller
(jfm@aeronomie.be)

the model predictions and a set of atmospheric observations. This adjustment requires first to define the emission parameters to be optimized, and then to minimize a scalar function of these parameters (the cost function) which quantifies the discrepancy between the model and the observations. It is implicitly assumed that the relationship between surface fluxes and atmospheric abundances is reasonably well predicted by the model, so that the biases between the model and the data are mostly due to errors in the emission inventories.

The inversion method to be used depends on the type of the constituent under consideration. When the atmospheric concentrations are linearly dependent on their emissions, as is the case for inert (CO₂) or long-lived gases (e.g. CH₄), Green's function and mass-balance methods or the linear Kalman filter scheme are appropriate to perform tracer inversion. In addition, the calculation of a posteriori errors is straightforward and exact for these methods, in the sense that errors assigned to the inputs propagate through the whole of the inversion (see the review paper by Enting, 2000, and references therein). Mass balance methods have been applied in the case of CO₂ (Enting and Mansbridge, 1989; Ciais et al., 1995) and CH₄ (Butler, 2004) inversion studies. The synthesis approach has been used by Enting et al. (1995), Fan et al. (1998) for CO₂ or more recently, by Peylin et al. (2000), and Rodenbeck et al. (2003a). When the linearity condition between emissions and atmospheric abundances does not hold, as happens for reactive trace gases like the ozone precursors, the aforementioned techniques for optimizing the emissions are no longer exact. However, they can still be applied, as long as only weak non-linearities are present, as in the CO inversion studies conducted recently by Bergamaschi et al. (2000a) and Pétron et al. (2002) in a global scale, or by Palmer et al. (2003) in a continental scale.

The adjoint model technique, however, has two important advantages compared to the aforementioned techniques: it is able to address any non-linear problem, and it can handle any large number of control parameters. This technique relies on the exact evaluation of the gradient of the cost function with respect to the control variables by the adjoint model. Its main limitations are that it requires important programming efforts and large computing resources, and that it does not provide an exact evaluation of the errors on the optimized emissions. For further information, the reader is referred to the review article by Giering (2000).

Adjoint models have been used to explicitly calculate inverse base functions for a given set of observations (as applied e.g. by Houweling et al., 1999; Kaminski et al., 1999) with subsequent analytical solution of the optimization problem or alternatively, as in this study, in an iterative approach. A similar iterative approach is also used in the 3d-var/4d-var data assimilation techniques (e.g. Elbern and Schmidt, 2001; Errera and Fonteyn, 2001); here, the analysis problem consists in determining initial conditions for the model such that the subsequent evolution minimizes the misfit with the observations.

A number of studies on inverse modelling of emissions using the adjoint model technique have been successfully conducted during the last years either on a regional (Menut et al., 2000), continental (Elbern et al., 2000), or a global scale (Kaminski et al., 1999; Rodenbeck et al., 2003b). However, in past inversion studies only one chemical compound was optimized at a time, and the impact of the predicted emission changes on the chemical lifetime of the compound was usually neglected. In the present study, we address the problem of the simultaneous inversion of emissions of different chemical species, using the global CTM IMAGES (Müller and Brasseur, 1995) and an adjoint modelling framework including transport and chemistry.

The innovative features of the proposed inversion scheme are twofold. First, the emissions of different chemical species can be simultaneously optimized while taking their chemical interactions into account, through the chemical feedbacks of the CO-NO_x-NMVOCs-OH system. In addition, as different species may have common sources (like biomass burning), the information obtained from measurements of a given compound can be used to constrain the sources of other species, which are emitted but not necessarily observed. Multi-compound inversion offers, therefore, an alternative and appealing approach, provided that a large set of high quality measurements of different species is available and the computational cost required to perform the minimization is not prohibitive. The feasibility of the proposed method will be demonstrated, and its skills but also its limitations to predict improved global emission rates will be highlighted throughout the remainder of the article.

The paper is organized as follows. The IMAGES model is briefly described in Sect. 2. The inversion technique, the specification of the control parameters used in the present study, as well as a method for estimating the a posteriori errors on the control variables are thoroughly discussed in Sect. 3. Section 4 describes the different observational datasets (ground-based networks, satellite observations and aircraft campaigns) used to constrain the control parameters. Section 5 gives the results of the inversion studies and explores their main features. The sensitivities of the results to different assumptions are also presented and investigated. Comparisons of the inversion results to independent observations are discussed in Sect. 6 and a posteriori error estimates on the control parameters are given in Sect. 7. Section 8 places the results in the context of previous studies. The concluding section focuses on the advantages gained from using multi-compound inversion, the limitations of the method, as well as possibilities for future improvements.

2 The IMAGES model

IMAGES is a global three-dimensional chemical transport model of the troposphere that provides the global distribution of 59 chemical constituents between the Earth's surface

and the pressure level of 50 hPa or approximately 22.5 km of altitude (Müller and Brasseur, 1995). Recent updates and improvements will be discussed later in this section. We also give a brief outline of the major features of the model; for further details see Müller and Brasseur (1995).

IMAGES is run at a resolution of 5° in latitude and longitude with 25 vertical σ -levels and a time step equal to 6 hours. It simulates the concentrations of 40 long-lived (transported) and 19 short-lived chemical compounds through a chemical mechanism including 133 gas-phase reactions, 29 photodissociations, and 3 heterogeneous reactions on the surface of sulfate aerosols. The chemical mechanism is described in full detail in the following subsection and in the Appendix. The chemical solver is an adaptation of the quasi-steady state approximation of Hesstvedt et al. (1978). Advection is represented using a semi-Lagrangian transport scheme (Smolarkiewicz and Rasch, 1991) driven by monthly mean climatological winds derived from a global analysis of ECMWF fields for the period 1985–1989. Interannual variability of the meteorological parameters is not considered in this study. Note that, due to the use of monthly averaged winds, the model is unable to reproduce synoptic-scale variations of the concentration fields. The surface pressure, temperature and humidity fields are also climatological averages derived from the same ECMWF analysis. The horizontal velocities have been adjusted in order to ensure that the vertically integrated mass fluxes are consistent with the surface pressure field, by adapting the methodology proposed by Rotman et al. (2003). The mixing of the chemical compounds resulting from the temporal variability of the winds is introduced in the model via horizontal and vertical diffusion coefficients, estimated using the ECMWF wind variances. Turbulent mixing in the planetary boundary layer (PBL) is also parameterized as vertical diffusion. Convection is approached following the Costen et al. (1988) parameterization. The cloud updrafts are distributed according to the monthly averaged climatological (1983–2001) distributions of the cumulonimbus fractional cover provided by the International Satellite Cloud Climatology Project (ISCCP) (“D2” dataset, see Rossow et al., 1996, and <http://isccp.giss.nasa.gov/products/isccpDsets.html>). The rainout/washout scheme for soluble species, also based on the ISCCP-D2 dataset, has been modified from the original version, as described in Rodriguez and Dabdub (2003).

The model uses diurnally averaged photolysis rates, and calculates diurnally averaged concentrations. The diurnal variations in the photorates and in the concentrations are taken into account through correction factors on the photorates and on the chemical kinetic rates, as described in Müller and Brasseur (1995). The correction factors are calculated from full diurnal cycle calculations, which are performed off-line in the present version of the model.

Model transport has been evaluated against ²²²Rn and ⁸⁵Kr measurements in Müller and Brasseur (1995) and in Friedl (1997). The model results have been compared to

other CTMs in Kanakidou et al. (1998), and with various aircraft measurements in Thakur et al. (1999), Emmons et al. (2000), and Law et al. (2000). A more recent comparison with other chemistry-transport models, as well as with station data, ozone sondes, and GOME NO₂ tropospheric columns has been presented in Savage et al. (2003).

Model runs include a spin-up time of 4 months, starting on 1 September. The model results are confronted to observations between 1 January and 31 December of the second year.

2.1 Chemistry and photolysis rates

The chemical mechanism and kinetic rates are given in the Supplement (<http://www.atmos-chem-phys.org/acp/5/1157/acp-5-1157-sp.pdf>). Rate constants for most reactions have been updated following DeMore et al. (1997), Sander et al. (2000), Horowitz et al. (2003), and Tyndall et al. (2001).

The degradation mechanism of ethane, propane, ethylene, propylene, isoprene, terpenes and a lumped compound OTHC, intended to be a surrogate for the other hydrocarbons has been updated following Horowitz et al. (2003) and Atkinson et al. (1999). The OTHC + OH-reaction rate constant at 298 K is taken equal to the average OH-reaction rate of NMVOCs, weighted by their anthropogenic emissions (Middleton et al., 1990). The temperature dependence of the reaction is as for *n*-C₄H₁₀ + OH (Horowitz et al., 2003). The isoprene oxidation mechanism has been considerably modified from the scheme used in Müller and Brasseur (1995) and is now based on Horowitz et al. (2003). The yield of gaseous products in the reactions of α -pinene is assumed to be 85% on a carbon basis, and the oxidation mechanism follows the isoprene mechanism. The yield of acetone from the oxidation of propane by OH is equal to 0.82 mol mol⁻¹ in the mechanism. The production of acetone from higher alkanes is neglected, although it could represent a significant source, on the order of 7 Tg/yr globally (Jacob et al., 2002). Acetone production from terpenes is not considered here, since it is treated as a direct surface source of acetone in the model. The oxidation of ONITR (surrogate for the reactive organic nitrates, mostly from isoprene) by OH follows Horowitz et al. (2003), except that nitric acid is produced (instead of NO₂), since it is a more likely product in the OH-addition pathway of alkyl nitrates (Atkinson, 1994).

The heterogeneous reactions of N₂O₅, NO₃, HO₂ on sulfate aerosols are represented as pseudosecond-order reactions between the species and particulate sulphate. Their rates are calculated following the assumptions of Dentener and Crutzen (1993) on the particle composition (NH₄H₂SO₄) and size distribution. The reaction probabilities are those recommended in Jacob (2000). The heterogeneous reactions of other compounds (e.g. NO₂, O₃, HNO₃) are neglected, as well as the reactions on other aerosol types (e.g. dust).

The photodissociation frequencies (J-values) in the model are interpolated from tabulated values calculated using the

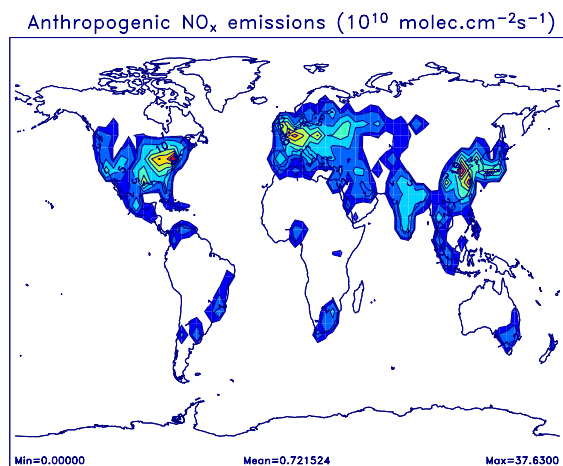


Fig. 1. A priori NO_x anthropogenic emissions for 1997.

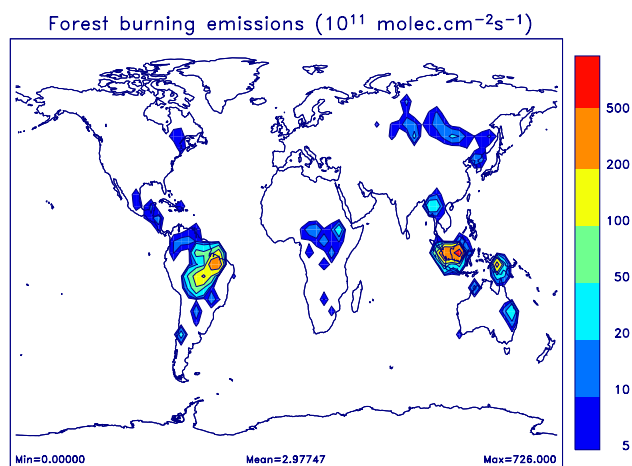


Fig. 3. A priori forest burning emissions of CO₂ for 1997.

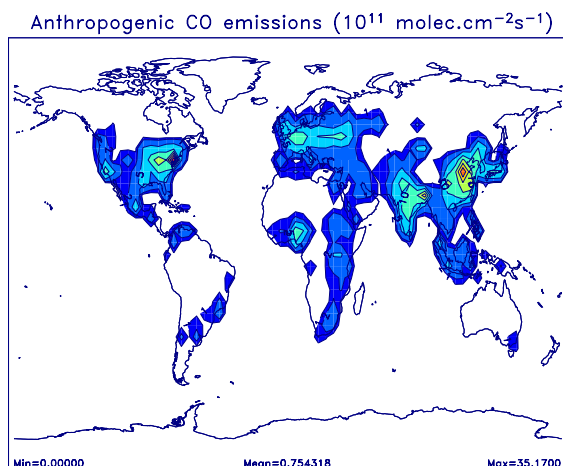


Fig. 2. A priori CO anthropogenic emissions for 1997.

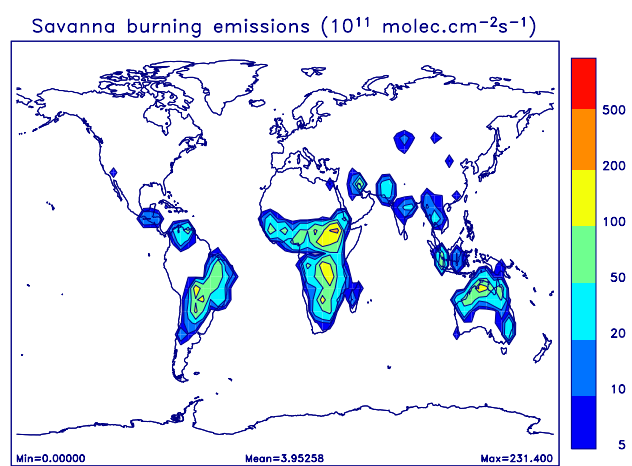


Fig. 4. A priori savanna burning emissions of CO₂ for 1997.

TUV photolysis calculation package (Madronich and Flocke, 1998), which is based on the pseudo-spherical 8-stream discrete ordinate method for radiative transfer (Stamnes et al., 1988). The model calculates J values at each time step and each grid point by linearly interpolating the logarithm of J from the table. References for absorption cross sections and quantum yields are given in the Supplement (<http://www.atmos-chem-phys.org/acp/5/1157/acp-5-1157-sp.pdf>). The table includes J -values calculated for 12 altitudes (0, 1, 2, 3, 5, 7, 9, 12, 16, 18, 21, 24 km), 5 total ozone columns (0.5, 0.75, 1, 1.5 and 2 times the standard profile taken from the US Standard Atmosphere, 1976), 6 temperature profiles defined by their 500-hPa and 200-hPa temperatures, 8 zenith angles (secant of angle = 1, 1.3, 1.6, 2, 3, 6, 12, 50), 3 surface albedos (0.05, 0.2, 0.5), 3 cloud optical depths (0, 5, 10) and 3 aerosol optical depths (0, 1, 2). In these calculations, clouds are assumed to extend between 2 and 6 km of altitude, and their horizontal distributions are climato-

logical monthly averages from the ISCCP-D2 climatology. Aerosols are distributed in the horizontal according to the TOMS total aerosol optical thickness (AOT) climatology developed by Torres et al. (1998) (<http://toms.gsfc.nasa.gov/aerosols/aot.html>). Comparisons of the TOMS values with the ground-based measurements of the AERONET network (Torres et al., 2002) indicate a fair agreement between both datasets. TOMS captures the distribution patterns of the most predominant aerosol types, although the loss of spatial coverage due to clouds and snow leads to a likely underestimation of total AOT poleward of about 35° in wintertime in our model. The vertical distribution of the aerosol total optical thickness assumes an exponential decrease in the vertical with a 3 km scale height. A unique value of 0.9 is adopted for the single scattering albedo of aerosols. Using this rather crude average might lead to an overestimation of the radiative impact of sulfate and sea salt. However, the resulting impact of aerosols on photolysis rates (e.g., $J(\text{O}^1\text{D})$) is calculated

Table 1. A priori global emissions of CO and NO_x for 1997. CO is expressed in TgCO/yr, and NO_x in TgN/yr.

Species	Source		Total	
CO	Anthropogenic	Technological	309	571
		Biofuel	237	
		Agr. waste burning	25	
	Vegetation fires	Tropical forest	207	409
		Non-tropical	16.8	
		Savanna	185.2	
	Biogenic		160	
	Oceans		20	
	Total		1160	
NO _x	Anthropogenic	Technological	24.6	30.89
		Aircrafts	0.64	
		Ships	2.92	
		Biofuel	2.41	
		Agr. waste burning	0.32	
	Vegetation fires	Tropical forest	1.47	6.88
		Non-tropical	0.22	
		Savanna	5.19	
	Soils		8	
	Lightning		3	
	Total		48.77	

to be similar to the sensitivity calculated by Martin et al. (2003) using the GOCART model and a more comprehensive treatment of radiative effects.

2.2 Emissions

The surface emissions for the year 1997 are summarized in Tables 1, 2 and 3.

Technological sources include emissions from fossil fuel burning (oil, gas, coal), industrial activities and waste disposal. Biomass burning accounts for forest and savanna fires, biofuel use and agricultural waste burning. Continental biogenic sources include the emissions of hydrocarbons by vegetation as well as the release of NO_x from soils. The model also accounts for oceanic emissions.

Emissions from technological sources, biofuel use and agricultural waste burning are based on the EDGAR v3.2 inventory (Olivier and Berdowski, 2001; Olivier et al., 2001, 2003; Peters and Olivier, 2003), see also <http://arch.rivm.nl/env/int/coredata/edgar/>). The 1997 inventory has been compiled by combining the inventory for 1995 with regional trend data for various sources (see Peters and Olivier, 2003, for details on this approach). The seasonal variation of technological emissions is determined from the seasonal variation of fossil fuel consumption and production and from the temperature dependence of vehicle emissions following Müller (1992).

The distribution of vegetation fires has been provided by Olivier et al. (2003). This inventory is based on the active fire counts from the Along Track Scanning Radiometer (ATSR)

Table 2. A priori 1997 global emissions of C₂H₆, C₃H₈, (CH₃)₂CO, OTHC, isoprene and monoterpenes expressed in Tg/yr.

Species	Source		Total	
C ₂ H ₆	Anthropogenic	Technological	5.2	7.1
		Biofuel	1.6	
		Agr. waste burn.	0.3	
	Veget. fires	Tropical forest	2.4	3.4
		Non-tropical	0.1	
		Savanna	0.9	
	Biogenic		1	
	Oceans		1	
	Total		12.5	
C ₃ H ₈	Anthropogenic	Technological	7.2	7.8
		Biofuel	0.5	
		Agr. waste burn.	0.1	
	Veget. fires	Tropical forest	0.3	0.5
		Non-tropical	0.0	
		Savanna	0.2	
	Biogenic		2	
	Oceans		1.3	
	Total		11.6	
(CH ₃) ₂ CO	Anthropogenic	Technological	0.3	0.5
		Biofuel	0.03	
		Agr. waste burn.	0.2	
	Veget. fires	Tropical forest	1.2	2.6
		Non-tropical	0.1	
		Savanna	1.3	
	Biogenic		24.2	
	Oceans		5	
	Total		32.3	
OTHC	Anthropogenic	Technological	111.2	138.8
		Biofuel	24.9	
		Agr. waste burn.	2.7	
	Veget. fires	Tropical forest	22.4	44.1
		Non-tropical	2.5	
		Savanna	19.2	
Total		182.9		
C ₅ H ₈	Veget.		567.9	
C ₁₀ H ₁₆	Veget.		144	

sensor on board the ERS-2 satellite (Olivier et al., 2003). The distribution of burnt biomass follows the ATSR fire counts over the period 1997–2001. The emissions are scaled in such a way that the total CO₂ emissions averaged over this period match the global annual emissions estimate provided by Hao and Liu (1994). The emissions of chemical species other than CO₂ are then computed using the emission ratios provided by Andreae and Merlet (2001). The Figs. 1, 2, 3 and 4 display the 1997 NO_x and CO anthropogenic and biomass burning emissions.

Biogenic emissions of isoprene and monoterpenes are taken from Guenther et al. (1995), for CO, C₂H₆, C₂H₄, C₃H₆ from Müller and Brasseur (1995), for C₃H₈ from Müller and Brasseur (1999), and for NO_x from Yienger

Table 3. A priori 1997 global emissions of C₂H₄, C₃H₆, and CH₂O expressed in Tg/yr.

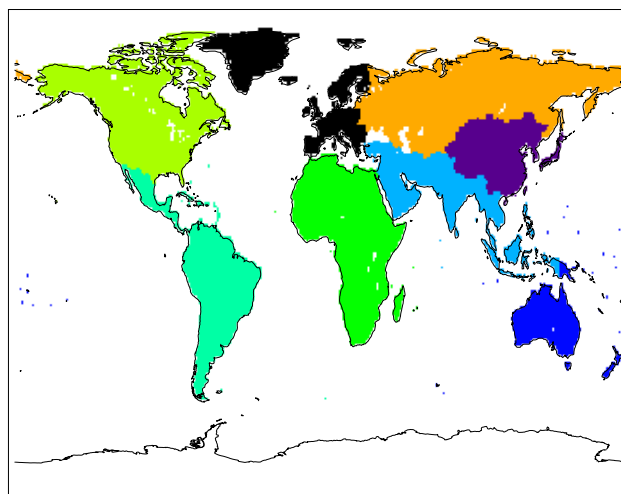
Species	Source		Total	
C ₂ H ₄	Anthropogenic	Technological	1.3	4.9
		Biofuel	3.2	
		Agr. waste burn.	0.4	
	Veget. fires	Tropical forest	3.9	6.4
		Non-tropical	0.2	
		Savanna	2.3	
	Biogenic			5
	Oceans			9.7
	Total			26
C ₃ H ₆	Anthropogenic	Technological	0.6	2.4
		Biofuel	1.5	
		Agr. waste burn.	0.3	
	Veget. fires	Tropical forest	1.1	1.9
		Non-tropical	0.1	
		Savanna	0.7	
	Biogenic			1
Oceans			11.8	
Total			17.1	
CH ₂ O	Anthropogenic	Technological	0.4	1.2
		Biofuel	0.5	
		Agr. waste burning	0.3	
	Veget. fires	Tropical forest	2	2.9
		Non-tropical	0.2	
		Savanna	0.7	
	Total			4.1

and Levy (1995). The biogenic emissions of acetone are distributed as the monoterpene emissions of Guenther et al. (1995), and their global total follows Wang et al. (1998) and Müller and Brasseur (1995). Ocean emissions of CO and NMVOCs are distributed according to the ocean emission of CO derived by Erickson (1989).

The lightning source of NO_x, globally scaled to 3 TgN/yr, is distributed horizontally according to Price et al. (1997), and vertically following Pickering et al. (1998). Global aircraft emissions of NO_x amount to 0.64 TgN/yr in 1997 (Olivier, J., personal communication), their spatial distribution and seasonality follow the NASA compilation for 1992 (Baughcum et al., 1996; Friedl, 1997). Aircraft emissions of CO and hydrocarbons are ignored, as they represent a negligible contribution to the budget of these species. Dry deposition velocities are taken from Müller and Brasseur (1995).

3 The inversion method

The mathematical and technical aspects of the inversion scheme are presented below. The control parameters used in the inversion, their a priori global fluxes and the errors associated to them are given in Tables 4 and 5.

**Fig. 5.** Regions used for the inversion of anthropogenic emissions (Table 4).

3.1 Optimizing emission distributions

Let us consider a model $F_t : \mathbf{R}^n \rightarrow \mathbf{R}^n$, which describes the time evolution of an initial state $s_0 \in \mathbf{R}^n : s(t) = F_t(s_0)$. In our case, the initial state s is obtained by the values of trace gases concentrations at the model gridpoints; the values of surface fluxes provided by emission inventories serve as boundary conditions in our model.

As discussed in Sect. 1, our aim is to adjust the surface fluxes, so that the predicted state $s(t)$ exhibits minimal deviation from the observed state $y(t)$. In practice, the observed state is known for a discrete set of times $\{t_1, \dots, t_p\}$, and locations. Since these locations generally do not coincide with the model grid, interpolations are required to compare these observations with the model. Let the observations be $y_i = y(t_i) \in \mathbf{R}^k, i = 1, \dots, p$ and let $\pi : \mathbf{R}^n \rightarrow \mathbf{R}^k$ be the projection mapping the model state space onto the observation space. This operator vanishes on all entries in a vector of \mathbf{R}^n , except for those for which observations are available.

Let $\Phi_j(x, t)$ be the a priori emission and deposition velocity distributions used in the model, where $j=1, \dots, m$ denote the different emission (or deposition) categories, and x, t the space (latitude, longitude, altitude) and time (month) variables. For example, the a priori emissions for a given species can be written as:

$$G_0(x, t) = \sum_{j=j_1}^{j_2} \Phi_j(x, t), \quad (1)$$

where j denotes the emission (or deposition) processes. The inversion scheme consists in bringing the model predictions as close as possible to a set of observations, by varying a set of dimensionless control parameters f_j , in a way that the

Table 4. Control parameters used in the inversion, except for the biomass burning related parameters displayed in Table 5, and values of the corresponding a priori emissions (Tg/yr) and uncertainty parameters Δf_j .

Control parameters f_j		A priori global fluxes (Tg/yr)	Δf_j	
CO anthropogenic emissions	N. America	90.4 CO	0.5	
		19 OTHC		
	S. America	40.3 CO	0.7	
		10.3 OTHC		
	Africa	76.5 CO	0.7	
		10.2 OTHC		
	Europe	46.8 CO	0.5	
		17.3 OTHC		
	Far East	128.6 CO	0.7	
		17.5 OTHC		
	Former S. U.	37.6 CO	0.7	
		13.3 OTHC		
South Asia	145.8 CO	0.7		
	26.3 OTHC			
Oceania	5.0 CO	0.5		
	1.4 OTHC			
CO/VOC natural emissions	Biogenic CO/VOC	160 CO	1	
		567.9 ISOP		
		144 APIN		
CO dep.velocity	Oceanic CO	20	1	
NO _x anthropogenic emissions	NO _x anthropogenic emissions	-230.8	0.7	
		N. America	6.24	0.5
		S. America	2.00	0.7
		Africa	1.53	0.7
		Europe	4.19	0.5
		Far East	5.76	0.7
		Former S.U.	2.46	0.7
		South Asia	4.64	0.7
		Oceania	0.49	0.5
		Ships	2.92	0.7
NO _x natural emissions	NO _x natural emissions	Lightn.-Tropics	2.40	1
		Lightn.-Extratrop.	0.60	1
		Soils-Tropics	4.93	1
		Soils-Extratrop.	3.07	1
NO _x dep.velocity		-4.9	0.7	

optimized emissions for the given species are expressed by the formula

$$G(x, t) = \sum_{j=j_1}^{j_2} \exp(f_j) \Phi_j(x, t). \quad (2)$$

Note that exponentiation is used to ensure the positiveness of the optimized fluxes. This choice leads, however, to non-Gaussian errors on the fluxes, when a Gaussian probability distribution is assumed for the errors on the control parameters f_j .

Table 5. Biomass burning related control parameters used in the inversion, and values of the corresponding a priori emissions (Tg/yr) and uncertainty parameters Δf_j .

Control parameters f_j		A priori global fluxes (Tg/yr) for 1997	Δf_j
CO: vegetation fires emission factors	Trop. forest fires	207.0	0.7
	0.099 mol./mol.CO ₂		
	Savanna fires		
NO _x : vegetation fires emission factors	0.0619 mol./mol.CO ₂	185.2	0.7
	Non-trop. for. fires		
	0.102 mol./mol.CO ₂		
Forest fires: burnt biomass (expressed as C)	Trop. forest fires	1.47	0.7
	1.41·10 ⁻³ mol./mol.CO ₂		
	Savanna fires		
	3.47·10 ⁻³ mol./mol.CO ₂		
Savanna fires: burnt biomass (expressed as C)	Non-trop. for. fires	5.19	0.7
	2.66·10 ⁻³ mol./mol.CO ₂		
	Trop. Asia/Oceania		
	477.1		
Forest fires: burnt biomass (expressed as C)	Trop. America	373.3	1
	Africa		
	45.2		
	70.7		
Savanna fires: burnt biomass (expressed as C)	North Africa	354.4	1
	South Africa		
	286.1		
	296.4		
Savanna fires: burnt biomass (expressed as C)	America	345.7	1
	Asia-Australia		

Given that G provides the surface boundary conditions in the model, then the state $s(t)$ is a function of the vector f ; we will set $s(t_i) = S_i(f)$.

The control parameters chosen for the inversion are displayed in Tables 4 and 5. They include the annual emissions of CO and NO_x over large geographical areas and for different broad source categories: (1) anthropogenic emissions of CO and NO_x in 8 regions (see Fig. 5) (2) NO_x emissions from ships (3) biomass burnt in forest and savanna fires in 4 regions (4) biomass burning emission factors for CO and NO_x (5) natural emissions (vegetation, soils, lightning), and (6) CO and NO_x deposition velocities.

Note that in the case of vegetation fire emissions of CO and NO_x, changes between a priori and optimized emissions result from the combined optimizations of biomass burnt and emission factors. For instance, the a posteriori savanna fire emissions of a compound are calculated by multiplying their a priori distribution by the exponentiated sum of the optimized control parameters corresponding to the region and to the species emission factor:

$$G_{sav}(x, t) = \exp(f_{EF,sav}) \sum_{\ell=\ell_1}^{\ell_4} \exp(f_\ell) \Phi_{\ell,sav}(x, t) \quad (3)$$

where $f_{EF,sav}$ is the optimized control variable corresponding to the savanna burning emission factor, f_ℓ ($\ell = \ell_1, \dots, \ell_4$)

are the optimized control variables corresponding to biomass burnt in savanna fires in four different regions (cf. Table 5), and $\Phi_{\ell, sav}(x, t)$ are the a priori savanna fire emissions for the species considered.

The optimization algorithm proceeds as follows. In the first step, the model calculates the state $s(t_i)$ for all t_i (monthly means), with $f_j=0, \forall j$. From this forward model simulation, the cost function $J : \mathbf{R}^m \rightarrow \mathbf{R}$, which quantifies the bias between the model prediction and the observations, is calculated:

$$\begin{aligned} J(\mathbf{f}) &= J_{obs}(\mathbf{f}) + J_B(\mathbf{f}) \\ &= \frac{1}{2} \sum_{i=1}^p (\mathbf{H}_i(\mathbf{f}) - \mathbf{y}_i)^T \mathbf{E}^{-1} (\mathbf{H}_i(\mathbf{f}) - \mathbf{y}_i) \\ &\quad + \frac{1}{2} (\mathbf{f} - \mathbf{f}_B)^T \mathbf{B}^{-1} (\mathbf{f} - \mathbf{f}_B), \end{aligned} \quad (4)$$

where \mathbf{E} , \mathbf{B} are the matrices of error estimates on the observations and the emission parameters, respectively, $\mathbf{H}_i = \pi \circ \mathbf{S}_i$, \mathbf{f}_B is the first guess value for the control parameters (taken equal to zero as previously stated), and T means the transpose. The first contribution, J_{obs} , measures the bias between the forward model predictions and the chemical observations, whereas the second contribution, J_B , is a regularization term needed to ensure that the problem has a unique solution and to prevent a posteriori emissions from being too different from their initial guess values.

We define the vector $\boldsymbol{\epsilon}_o$ of observation errors and the vector $\boldsymbol{\epsilon}_B$ of the a priori errors on the emission parameters by the following relations:

$$\boldsymbol{\epsilon}_o = \mathbf{y} - \mathbf{H}(\mathbf{f}_{true}), \quad \boldsymbol{\epsilon}_B = \mathbf{f}_{true} - \mathbf{f}_B. \quad (5)$$

Here, \mathbf{f}_{true} is the best possible representation of the vector of control variables, and $\mathbf{H}(\mathbf{f}_{true})$ the vector of \mathbf{R}^p whose components are $\mathbf{H}_i(\mathbf{f}_{true}), i=1, \dots, p$. The vector $\boldsymbol{\epsilon}_o$ includes errors produced during the observation process as well as errors on the operator \mathbf{H} . Since it is supposed that the observation errors as well as the background errors are uncorrelated, the matrices \mathbf{E} and \mathbf{B} are diagonal; their diagonal terms are the variances of the observation and a priori background errors, respectively. More precisely, the a priori background errors on the control parameters are defined as

$$\widetilde{\Delta f_j} = \Delta f_j / \Omega = \sqrt{B_{jj}}, \quad (6)$$

where the values of Δf_j are given in Tables 4 and 5, B_{jj} are the diagonal elements of the matrix \mathbf{B} , and Ω is a regularization parameter adjusted to ensure an adequate weighting of J_{obs} and J_B in Eq. (4). Its value is initially taken equal to 5. The value of Ω will be modified in sensitivity tests presented in Sect. 5. The values of Δf_j range from 0.5 for the best constrained emissions (i.e. anthropogenic emissions in Western Europe, North America and Oceania) to 1 for highly uncertain emission categories (e.g. natural emissions).

In the next step, the adjoint of the model (see next subsection) is used to calculate the gradient of J with respect

to the parameter vector \mathbf{f} . Subsequently, applying a suitable iterative descent algorithm on J , which makes use of this gradient, we obtain a new estimate for the parameter vector \mathbf{f} . The latter is used as input for the next simulation, and this algorithm continues until J reaches its minimum.

The gradient $(\nabla J)_f$ of the cost function with respect to the control variables is calculated as follows. By straightforward calculation, we obtain that if $I : \mathbf{R}^m \rightarrow \mathbf{R}$ is a scalar function of the form:

$$I(\mathbf{x}) = \frac{1}{2} \boldsymbol{\alpha}(\mathbf{x})^T \mathbf{K} \boldsymbol{\alpha}(\mathbf{x}), \quad \forall \mathbf{x} \in \mathbf{R}^m, \quad (7)$$

where $\boldsymbol{\alpha}$ is a differentiable vector function $\boldsymbol{\alpha} : \mathbf{R}^m \rightarrow \mathbf{R}^n$, \mathbf{K} a symmetric constant $n \times n$ matrix, and T means the transpose, then the gradient $(\nabla I)_x$ is given by

$$(\nabla I)_x = (D\boldsymbol{\alpha})_x^T \mathbf{K} \boldsymbol{\alpha}(\mathbf{x}). \quad (8)$$

Here $(D\boldsymbol{\alpha})_x$, the derivative of $\boldsymbol{\alpha}$ at x is viewed as a linear transformation $\mathbf{R}^m \rightarrow \mathbf{R}^n$ (Jacobian matrix):

$$(D\boldsymbol{\alpha})_x = \begin{pmatrix} \frac{\partial \alpha_1}{\partial x^1}(\mathbf{x}) & \dots & \frac{\partial \alpha_1}{\partial x^m}(\mathbf{x}) \\ \vdots & & \vdots \\ \frac{\partial \alpha_n}{\partial x^1}(\mathbf{x}) & \dots & \frac{\partial \alpha_n}{\partial x^m}(\mathbf{x}) \end{pmatrix}. \quad (9)$$

Applying now formula (8) in the case of the cost function of Eq. (4), it is straightforward that:

$$\begin{aligned} (\nabla J)_f &= \sum_{i=1}^p (D\mathbf{H}_i)_f^T \mathbf{E}^{-1} (\mathbf{H}_i(\mathbf{f}) - \mathbf{y}_i) \\ &\quad + \mathbf{B}^{-1} (\mathbf{f} - \mathbf{f}_B) \end{aligned} \quad (10)$$

3.2 Adjoint code generation and minimizer

The cost function is an example of a complicated numerical algorithm consisting in a composition of differentiable mappings. Let us now examine how the gradient of this function can be calculated, by using Eq. (10).

Let us consider the general algorithm $A : \mathbf{R}^m \rightarrow \mathbf{R}^n$, which can be decomposed into $K \in \mathbf{N}$ steps, $A = A^K \circ \dots \circ A^1$, where $A^\ell : \mathbf{R}^{n_{\ell-1}} \rightarrow \mathbf{R}^{n_\ell}$, $Z^{\ell-1} \mapsto Z^\ell$, $\ell \in \{1, \dots, K\}$ are differentiable maps. Applying the chain rule of differentiation, we can write for the derivative of A at $X = X_0$:

$$(DA)_{X_0} = (DA^K)_{Z_0^{K-1}} \circ \dots \circ (DA^2)_{Z_0^1} \circ (DA^1)_{X_0}, \quad (11)$$

where we have used the notation $Z_0^\ell = (A^\ell \circ \dots \circ A^1)(X_0)$, $1 \leq \ell \leq K$, and the convention $Z_0^0 = X_0$. For the computation of multiple matrix products like in Eq. (11), we might either operate in forward mode, that is to calculate the product from the right to the left, or operate in reverse mode, from the left to the right. Taking the adjoint (transpose) of Eq. (11) we have:

$$(DA)_{X_0}^T = (DA^1)_{X_0}^T \circ \dots \circ (DA^K)_{Z_0^{K-1}}^T. \quad (12)$$

Therefore, the reverse mode in Eq. (11) operates in the direction of the forward mode in Eq. (12). This is the reason why the reverse mode is known as adjoint mode. Now, since

$$(D(A^K \circ \dots \circ A^\ell))_{Z_0^{\ell-1}} = (D(A^K \circ \dots \circ A^{\ell+1}))_{Z_0^\ell} \circ (DA^\ell)_{Z_0^{\ell-1}}, \quad K \geq \ell \geq 1, \quad (13)$$

we can write:

$$(D(A^K \circ \dots \circ A^\ell))_{Z_0^{\ell-1}}^T = (DA^\ell)_{Z_0^{\ell-1}}^T \circ (D(A^K \circ \dots \circ A^{\ell+1}))_{Z_0^\ell}^T. \quad (14)$$

This means that the derivative $(DA^\ell)_{Z_0^{\ell-1}}^T$ of the ℓ th component of A allows us to calculate the derivative of the composition $A^K \circ \dots \circ A^\ell$ ($k-\ell$ terms) from the derivative of the composition $A^K \circ \dots \circ A^{\ell+1}$ ($k-\ell-1$ terms). Based on Eq. (14), we can calculate the adjoint (transpose) of the model matrix, needed to derive the gradient of the cost function of Eq. (10), for all algorithm steps ℓ .

In our case, the adjoint model is derived directly from the numerical code of the IMAGES model. This code, viewed as a composition of functions, is differentiated by applying the chain rule, as previously described. Since application of the adjoint model reverses the execution order, the backward in time calculation requires the knowledge of the model state at each time step. For this reason, trace gases concentrations are stored on disk at every time step in the forward run (totalling approximately 14GB, when the model time step is equal to 1 day). Using this checkpointing scheme, the adjoint model reads these concentrations, and thus, long recomputations are avoided. The adjoint code is implemented using the automatic differentiation software TAMC (Giering and Kaminski, 1998; Giering, 1999). Nevertheless, despite the automatization provided by TAMC, adjoint code generation often requires a substantial amount of programming effort, due to redundant recomputations generated by the compiler; the elimination of these recomputations has involved important modifications of the forward and adjoint codes. Using 8 processors on a SGI Origin 3400 Batch server, the runtime is 15 min for a complete simulation of the forward model and 1 h for the adjoint one.

The cost function and the derivatives calculated in the forward and adjoint models respectively, are used as inputs in the minimization subroutine MIQN3 developed by Gilbert and Lemaréchal (1989). This minimizer solves unconstrained minimization problems using a variable storage quasi-Newton method, where the inverse Hessian matrix is updated by the inverse BFGS formula (see for example Nocedal and Wright, 1999, and the next subsection). The computation of the cost function and its gradient is then performed iteratively. The convergence criterion used in the optimization runs is that the norm of the gradient of the cost function after minimization is reduced by a factor of

1000 with respect to the initial one. The number of iterations needed to attain this criterion is variable, generally between 20 and 40. In most optimization runs, however, the minimization procedure has been continued after the convergence criterion was reached. These additional iterations were found to result in negligible changes, however. Note that the optimization includes the spin-up period (September 1996–December 1996), although the model is compared to the data only in 1997.

In order to determine whether the same solution is obtained when starting from different parameter values, several tests with different initial fluxes have been conducted. Although the number of iterations needed to reach convergence was variable, in all cases, the minimization is found to produce the same optimal solution. This indicates that despite the non-linearities, local minima are not found.

3.3 A posteriori error estimation

The relation between the inverse Hessian matrix of the cost function at the minimum and the a posteriori error estimates of the control parameters has been discussed in Thacker (1989) and Rabier and Courtier (1992). This result is briefly presented below, and adapted to the case of the IMAGES model. Next, the estimation of the a posteriori errors using the inverse BFGS algorithm and the DFP formula will be discussed.

Using the fact that in a euclidean space the Hessian matrix of a (scalar) function can be obtained as the derivative of the gradient of the function, we can write for the Hessian of the cost function:

$$\mathbf{Hess}(J)_f = [D(\nabla J)]_f = \sum_{i=1}^p (D^2 \mathbf{H}_i)_f^T \mathbf{E}^{-1} (\mathbf{H}_i(f) - y_i) + \sum_{i=1}^p (D\mathbf{H}_i)_f^T \mathbf{E}^{-1} (D\mathbf{H}_i)_f + \mathbf{B}^{-1} \quad (15)$$

It is clear that, when the model is linear, the second order term of the Hessian is zero. As long as the model is not too far from being linear, the Hessian of the cost function is well approximated by the first order term of Eq. (15) and the second derivative term is ignored.

The linearity assumption has been checked by evaluating the diagonal elements of the first and second order terms of the Hessian by finite differences on the forward model results. The second order term, which takes the non-linearities into account, is indeed found to be about one order of magnitude smaller than the first order term. Due to the expensive computational cost required in these calculations, this comparison is performed for only one optimization run (case study A, see Table 9). For the rest of this work, we will proceed with the linearized Hessian matrix.

By putting now $(\nabla J)_f=0$ in Eq. (10) and using Eq. (5), and taking into account that the observation and background errors are uncorrelated, we find that the expectation value

$\mathcal{E}[(f - f_{true})(f - f_{true})^T] = \tilde{\mathcal{E}}$, which represents the a posteriori error covariance matrix, is related to the Hessian of the cost function through the following relation:

$$\tilde{\mathcal{E}} = \left[\sum_{i=1}^p (D\mathbf{H}_i)_f^T \mathbf{E}^{-1} (D\mathbf{H}_i)_f + \mathbf{B}^{-1} \right]^{-1} = \mathbf{Hess}(J)_f^{-1}. \quad (16)$$

In the present study, two algorithms have been used in order to approximate the true Hessian matrix, based on the inverse BFGS and DFP updating formulas (e.g. Nocedal and Wright, 1999). Both algorithms start with an initial approximation of the inverse Hessian matrix $(\mathbf{H})_0$ (usually chosen to be a diagonal matrix, e.g., the identity matrix or the Hessian of the background term in the cost function, \mathbf{B}) and combine the most recently acquired information about the objective function with the existing knowledge embedded in the current Hessian approximation. Given a sequence $s_k = f_{k+1} - f_k$ and $y_k = (\nabla J)_{f_{k+1}} - (\nabla J)_{f_k}$, then the sequence of approximations to the inverse of the Hessian matrix \mathbf{H} can be generated either by the inverse BFGS update formula:

$$(\mathbf{H})_{k+1} = (\mathbf{H})_k + \frac{s_k s_k^T}{y_k^T s_k} - \frac{(\mathbf{H})_k y_k s_k^T}{s_k^T y_k} - \frac{s_k y_k^T (\mathbf{H})_k}{y_k^T s_k} + \frac{s_k y_k^T (\mathbf{H})_k y_k s_k^T}{s_k^T y_k s_k^T y_k}, \quad (17)$$

or by the DFP formula:

$$(\mathbf{H})_{k+1} = (\mathbf{H})_k + \frac{s_k s_k^T}{y_k^T s_k} - \frac{(\mathbf{H})_k y_k y_k^T (\mathbf{H})_k}{y_k^T (\mathbf{H})_k y_k}. \quad (18)$$

Both updates generate symmetric and positive definite approximations whenever the initial approximation $(\mathbf{H})_0$ is positive definite and $s_k^T y_k > 0$ (e.g. Nocedal and Wright, 1999).

Iterative application of the inverse BFGS or DFP formulas (Eqs. 17, 18) on the vectors f_k and $(\nabla J)_{f_k}$ calculated in the minimization procedure, provides an approximation of the inverse Hessian matrix. This estimation for the inverse Hessian is evaluated against finite difference calculations performed on the adjoint model. In order to obtain reliable results, the Hessian is calculated for different perturbations around the initial parameter vector. Although generally far too computationally demanding, this method has been applied in the case studies A and B of Table 9. The results will be compared and discussed in Sect. 7. The square roots of the diagonal elements of the inverse Hessian matrix correspond to standard errors for each control parameter of the model; the off-diagonal terms represent correlations between pairs of control parameters.

4 Observations

Three different types of observations are used as constraints in the case studies presented in the next section: ground-

based measurements of CO mixing ratios and CO vertically integrated columns, NO₂ tropospheric columns retrieved from a satellite instrument, and the global methane lifetime deduced from methylchloroform studies. In addition, aircraft campaign measurements of CO are used as independent observations in order to evaluate the inversion results. These observations are described below.

4.1 Ground-based measurements

a. CO mixing ratios are provided by the NOAA/CMDL global sampling network (Novelli et al. (1998, 2003)) and made freely available via ftp (ftp://140.172.192.211/ccg/co/flask/event). Data consist of CO volume mixing ratios, sampling and analysis information for each flask sample, for 47 sampling locations (described in Table 6) and 2 shipboard programs, the Pacific Ocean Cruise and the South China Sea Cruise. The site locations (shown in Fig. 8) have wide latitudinal as well as longitudinal coverage, although a majority of sites are located in the northern mid-latitudes. As the CMDL network was originally intended to monitor the atmospheric composition in unpolluted conditions, most sites are located in the remote atmosphere.

In the present study, continental sites situated above 2500 m a.s.l. (Plateau Assy, Niwot Ridge, Mt. Waliguan, Assekrem) are not taken into account in the inversion, since the model resolution does not allow to account for topographical heterogeneities. Furthermore, when measurements from neighbouring stations present similar concentrations and seasonal features (e.g. Alert, Svalbard, Mould Bay), we consider data from only one station in the calculation of the cost function (see Table 6), since the model errors (see below) at these stations are highly intercorrelated. For instance, among high-latitude southern hemisphere stations (Tierra Del Fuego, Palmer, Syowa, Halley, South Pole), only data from Tierra Del Fuego station have been taken into account for the inversion.

Contrary to previous inversion studies based on the same measurements (Pétron et al., 2002), we take into account CMDL data representing non-background conditions (i.e., samples contaminated due to winds blowing from the direction of areas likely to produce CO), since the model introduces no filtering. However, exceptional events with concentrations more than three times greater than the mean value calculated over the period 1997–2001, are considered exceptional, and are excluded from further analysis.

The error σ_{obs} associated to the data in the expression of the cost function, combines the standard deviation of the measurements around their monthly means with an assumed representativity/model error of 10%:

$$\sigma_{obs}^2 = \left(\frac{1}{n} \sum_{j=1}^n c_j^2 - \bar{c}^2 \right) + (0.10 \cdot \bar{c})^2 \quad (19)$$

where c_j are the detrended monthly concentrations, \bar{c} their monthly averages, and n their number. These errors are

Table 6. CMDL stations used in this study. Asterisks denote stations that are not used in the inversion to limit redundancy (see text for details). Double asterisks denote mountainous sites, also not taken into account in the inversion.

Location	Latitude	Longitude	Alt.(m)	Location	Latitude	Longitude	Alt.(m)
Alert, Canada (*)	82.45° N	62.52° W	210	St. Davids Head, Bermuda	32.37° N	64.65° W	30
Svalbard, Norway	78.90° N	11.88° E	475	Tudor Hill, Bermuda (*)	32.27° N	64.88° W	30
Mould Bay, Canada (*)	76.25° N	119.35° W	58	Sede Boker, Israel	31.13° N	34.88° E	400
Barrow, Alaska	71.32° N	156.60° W	11	Tenerife, Canary Islands	28.30° N	16.48° W	2360
Ocean Station M, Norway	66.00° N	2.00° E	7	Sand Island, Midway	28.22° N	177.37° W	4
Vestmannaeyjar, Iceland (*)	63.25° N	20.15° W	100	Key Biscayne, Florida	25.67° N	80.20° W	3
Baltic Sea, Poland	55.50° N	16.67° E	7	Assekrem, Algeria (**)	23.18° N	5.42° E	2728
Cold Bay, Alaska	55.20° N	162.72° W	25	Mauna Loa, Hawaii	19.53° N	155.58° W	3397
Mace Head, Ireland	53.33° N	9.90° W	25	C. Kumukahi, Hawaii	19.52° N	154.82° W	3
Shemya Island, Alaska (*)	52.72° N	174.10° E	40	Mariana Islands, Guam	13.43° N	144.78° E	2
Hegyhatsal, Hungary	46.95° N	16.65° E	344	Ragged Point, Barbados	13.17° N	59.43° W	45
Park Falls, Wisconsin	45.93° N	90.27° W	868	Christmas Island, Kiribati	1.7° N	157.17° W	3
Cape Meares, Oregon	45.48° N	123.97° W	30	Mahe Island, Seychelles	4.67° S	55.17° E	3
Sary Taukum, Kazakhstan	44.45° N	77.57° E	412	Ascension Island	7.92° S	14.42° W	54
Ulaan Uul, Mongolia	44.45° N	111.10° E	914	Tutuila, American Samoa	14.25° S	170.57° W	42
Black Sea, Romania	44.17° N	28.68° E	3	Easter Island, Chile	27.15° S	109.45° W	50
Plat. Assy, Kazakhstan (**)	43.25° N	77.88° E	2519	Cape Grim, Tasmania	40.68° S	144.68° E	94
Niwot Ridge, Colorado (**)	40.05° N	105.58° W	3475	Crozet Island	46.45° S	51.85° E	120
Wendover, Utah	39.90° N	113.72° W	1320	Tierra Del Fuego, Argentina	54.87° S	68.48° W	20
Terceira Island, Azores	38.77° N	27.38° W	40	Palmer St., Antarctica (*)	64.92° S	64.00° W	10
Tae-ahn Peninsula, Korea	36.73° N	126.13° E	20	Syowa St., Antarctica (*)	69.00° S	39.58° E	11
Mt. Waliguan, China (**)	36.29° N	100.90° E	3810	Halley St., Antarctica (*)	75.58° S	26.50° W	10
Dwejra Point, Malta	36.05° N	14.18° E	30	South Pole (*)	89.98° S	24.80° W	2810
Grifton, North Carolina	35.35° N	77.38° W	505	Cruise locations	see Fig. 8		

assumed to be mutually independent. Model errors include errors associated to the transport and chemical schemes used in the model, errors due to the use of monthly averaged climatological winds, as well as the aggregation errors related to the use of large regions. The measurement errors on the flask measurements are believed to be small, on the order of a few ppb (Novelli et al., 2003) and are therefore neglected. The first term of Eq. (19) corresponds to a variability error associated with the variability of the observations around their monthly averages. The error of the mean is small when the number of measurements is sufficiently large ($n \gg 10$). It is found to be most significant at the shipboard locations in the South China sea, where n is small and variability is large due to the proximity of large emission sources.

b. The CO vertical column abundances are provided by the column-measuring stations listed in Table 7. Ground-based FTIR (Fourier Transform InfraRed) instruments are used in all cases. Part of the data (for Ny-Alesund, Kitt Peak, Mauna Loa and Wollongong) is publicly available via the Network for the Detection of Stratospheric Change (NDSC) web site (<http://www.ndsc.ncep.noaa.gov>). The data for the NDSC stations of Jungfrauoch and Lauder were provided by Barret et al. (2003) and Jones et al. (2001), respectively. The CO columns at St Petersburg were provided by Makarova et al. (2001). The error associated to the data is calculated as in the

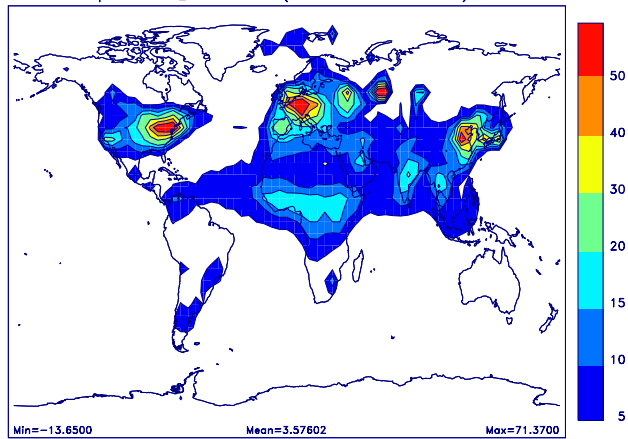
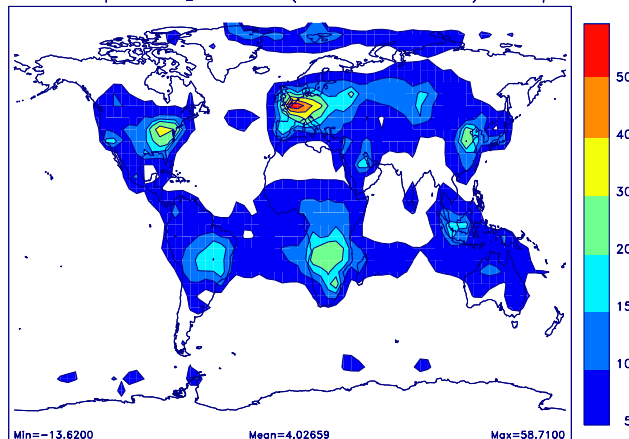
Table 7. Column-measuring stations used in this study.

Location	Latitude	Longitude	Altitude (m)
Ny-Alesund, Svalbard	78.92° N	11.92° E	20
St-Petersburg, Russia	59.88° N	29.83° E	35
Jungfrauoch, Switzerland	46.55° N	7.98° E	3578
Kitt Peak, Arizona	31.90° N	111.6° W	2090
Mauna Loa, Hawaii	19.54° N	155.62° W	3400
Wollongong, Australia	34.45° S	150.88° E	30
Lauder, New Zealand	45.04° S	169.68° E	370

case of CMDL stations, except that the error on the column retrieval by FTIR (on the order of 10%) must also be taken into account. The representativity error is therefore replaced by a 15% error which includes both the representativity and measurement errors.

4.2 Satellite observations

This study uses an improved version (V1b) (Richter et al., 2003) of the tropospheric NO₂ columns retrieved from measurements by the GOME spectrometer aboard the ERS-2 satellite (Richter and Burrows, 2002; Lauer et al., 2002).

GOME tropos. NO₂ column (10¹⁴ molec.cm⁻²) – March**Fig. 6.** GOME columns on March 1997.GOME tropos. NO₂ column (10¹⁴ molec.cm⁻²) – Sept.**Fig. 7.** GOME columns on September 1997.

The tropospheric excess method (TEM) was used in Richter and Burrows (2002) in order to separate tropospheric and stratospheric contributions of the total measured NO₂ column. It assumes that the stratospheric NO₂ column is longitudinally constant, and that the tropospheric NO₂ column amounts above a Pacific sector between 170° W to 180° W can be neglected. The first assumption is reasonable at low latitudes; however, close to the poles, longitudinal variations cannot be neglected and artifacts are introduced in the tropospheric columns. In version 1b, the subtraction of the stratospheric column uses the stratospheric NO₂ fields calculated by the SLIMCAT model, as described in Richter et al. (2003). This procedure reduces, but doesn't suppress, the errors associated to stratospheric variations. The next step to the data analysis is the correction of the tropospheric light path using the airmass factor calculation. In version 1b, these airmass factors are estimated using the tropospheric NO₂ distributions from the MOZART model. Due to the sun-synchronous orbit of ERS-2, measurements of GOME are performed around the same local time, 10:30 LT.

GOME measurements for the year 1997 are used in this study (http://www.doas-bremen.de/gome_no2_data.htm), gridded at the resolution of the model. To account for the fact that measurements take place at 10:30 LT, the diurnally averaged NO₂ concentrations calculated by the model are multiplied by a correcting factor expressing the ratio of the NO₂ concentration at 10:30 LT to the average NO₂ concentration. This ratio is calculated from the full diurnal cycle calculations, which are performed off-line.

The uncertainties on the tropospheric NO₂ columns derived from GOME measurements are related to the stratospheric subtraction procedure, to the calculation of airmass factors (i.e. on the NO₂ vertical profile, surface albedo, and aerosol loading), and to the presence of clouds (see Richter and Burrows, 2002 for a detailed error analysis; error estimation for a particular case has been done by Heland et al.,

2002). In order to calculate the NO₂ contribution to the cost function (Eq. 4), we take the observation errors to be equal to the maximum value of $5 \cdot 10^{14}$ molecule/cm² and 20% of the observed tropospheric column. As mentioned in Sect. 3.1, these errors include also model errors (i.e. errors associated with the design of the operator H); their quantification stands beyond the scope of this work. Due to the short lifetime of the NO_x family, the NO₂ concentrations predicted by the IMAGES model in remote areas (e.g. the oceans) are likely to be less reliable than in the vicinity of the emission regions. Therefore, only continental pixels are considered in the calculation of the cost function. Furthermore, snowy pixels and pixels located poleward of 60° are rejected, since the NO₂ retrieval is expected to be more uncertain in these areas.

4.3 Methane lifetime

Loss of atmospheric methane is dominated by its reaction with the hydroxyl radical (OH) in the troposphere. The loss term can be deduced from methylchloroform budget studies (see for example Prinn et al., 2001; Krol and Lelieveld, 2003). The tropospheric methane lifetime due to the reaction with OH is defined as the quotient of the total burden by the tropospheric loss by OH. In this study, the TAR recommended OH value is used (IPCC, 2001). This value is equal to 9.6 yr and is scaled from a methylchloroform OH lifetime of 5.7 yr. An additional term of the form

$$J_{\text{CH}_4} = A(\tau_{\text{CH}_4} - 9.6)^2 \quad (20)$$

is then added to the cost function, which quantifies the discrepancy between the tropospheric methane lifetime calculated by the model and the aforementioned value. In this equation, τ_{CH_4} is the tropospheric methane lifetime calculated by the model (yrs), and A is a constant suitably adjusted in order to ensure that the methane lifetime constraint is effective ($A=5 \cdot 10^3$).

Table 8. Campaign measurements used as independent observations in this study (Emmons et al., 2000).

Campaign	Period
PEM-Trop.-B	6/03–18/04 1999
SONEX	7/10–12/11 1997
POLINAT-2	19/09–25/10 1997
PEM-Trop.-A	15/08–5/10 1996
SUCCESS	15/04–15/05 1996
VOTE	20/01–19/02 1996
TOTE	6/12–22/12 1995
ACE-1	31/10–22/12 1995
OCTA-4	1/03–26/04 1994
PEM-West-B	7/02–14/03 1994
OCTA-2	19/08–1/09 1993
TRACE-A	21/09–26/10 1992
PEM-West-A	16/09–21/10 1991
ABLE-2B	1/04–13/05 1987

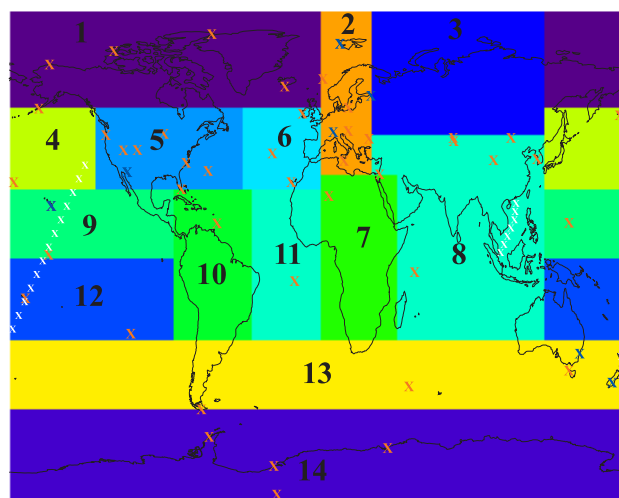
4.4 Aircraft campaigns

Tropospheric data from a number of aircraft campaigns compiled by Emmons et al. (2000) are used as independent observations to be compared to the optimized concentrations of carbon monoxide. The observations are averaged onto a 5°×5° horizontal grid with a 1-km vertical resolution. The data files, including the statistics of the data sets (number of measurements, minimum, maximum, mean, standard deviation) can be accessed through the data composites web site (http://acd.ucar.edu/~emmons/DATACOMP/camp_table.htm). For our purposes, CO measurements have been averaged over 14 large regions (Fig. 8). The model concentrations are averaged in the same regions taking into account the location of the measurements and the number of measurements at each location.

5 Inversion results

Five optimization studies were performed, using different combinations of the observational datasets described in the previous section, as shown in Table 9. The target period for the inversions is the year 1997. In these studies, CO (or CO and NO_x) emissions are constrained using 1997 observations, the a priori emissions being provided by the 1997 inventory summarized in Tables 4 and 5. In cases A, B and C the background errors on the control parameters are given by Eq. (6), with $\Omega=5$. In order to test the stability of the results, two sensitivity studies have been conducted, where the background errors are halved (case B1) and doubled (case B2).

In Fig. 9 we compare the a priori and (in black) and optimized (in red) monthly averaged CO measurements (mixing

**Fig. 8.** Red, blue and white crosses represent CMDL stations, column-measuring stations and ship measurements respectively (described in Sect. 4.1) and coloured regions are used for aircraft campaigns averages (see Sect. 4.4): 1. Boreal; 2. Europe; 3. Russia; 4. North Pacific; 5. N. America; 6. North-East Atlantic; 7. Africa; 8. South Asia; 9. N. Tropical Pacific; 10. S. America; 11. Tropical Atlantic; 12. S. Tropical Pacific; 13. Southern mid-latitudes; 14. Australia.**Table 9.** Summary of the case studies performed in the work.

Case study	Species optimized	Observations used	Factor Ω
A	CO	CMDL/columns	5
B	CO, NO _x	CMDL/col., GOME	5
B1	CO, NO _x	as in B	10
B2	CO, NO _x	as in B	2.5
C	CO, NO _x	as in B, CH ₄ lifetime	5

ratios and total columns) at selected sites. Only case A results are shown, since the differences between cases A, B and C are found to be very small at these sites.

As seen on Fig. 9, the optimization brings the model values much closer to the measurements at mid- and high latitudes, compared to the a priori. The increase in CO mixing ratios, on the order of 10 ppbv in summer and 40 ppbv or more in late winter, is mainly achieved by increasing anthropogenic emissions at these latitudes, as will be discussed later in detail. However, a significant bias remains between the model and the data during springtime at most remote stations of the Northern Hemisphere, which might suggest that the lifetime of CO is too short in the winter in the model. In case studies B and C, however, the slight reduction of the OH levels at these latitudes, leads to a small but discernible improvement in springtime CO mixing ratios. As the chemical lifetime of methane (8.63, 9.13 and 9.58 years in cases A, B and C, respectively) reflects primarily tropical OH concentrations, its

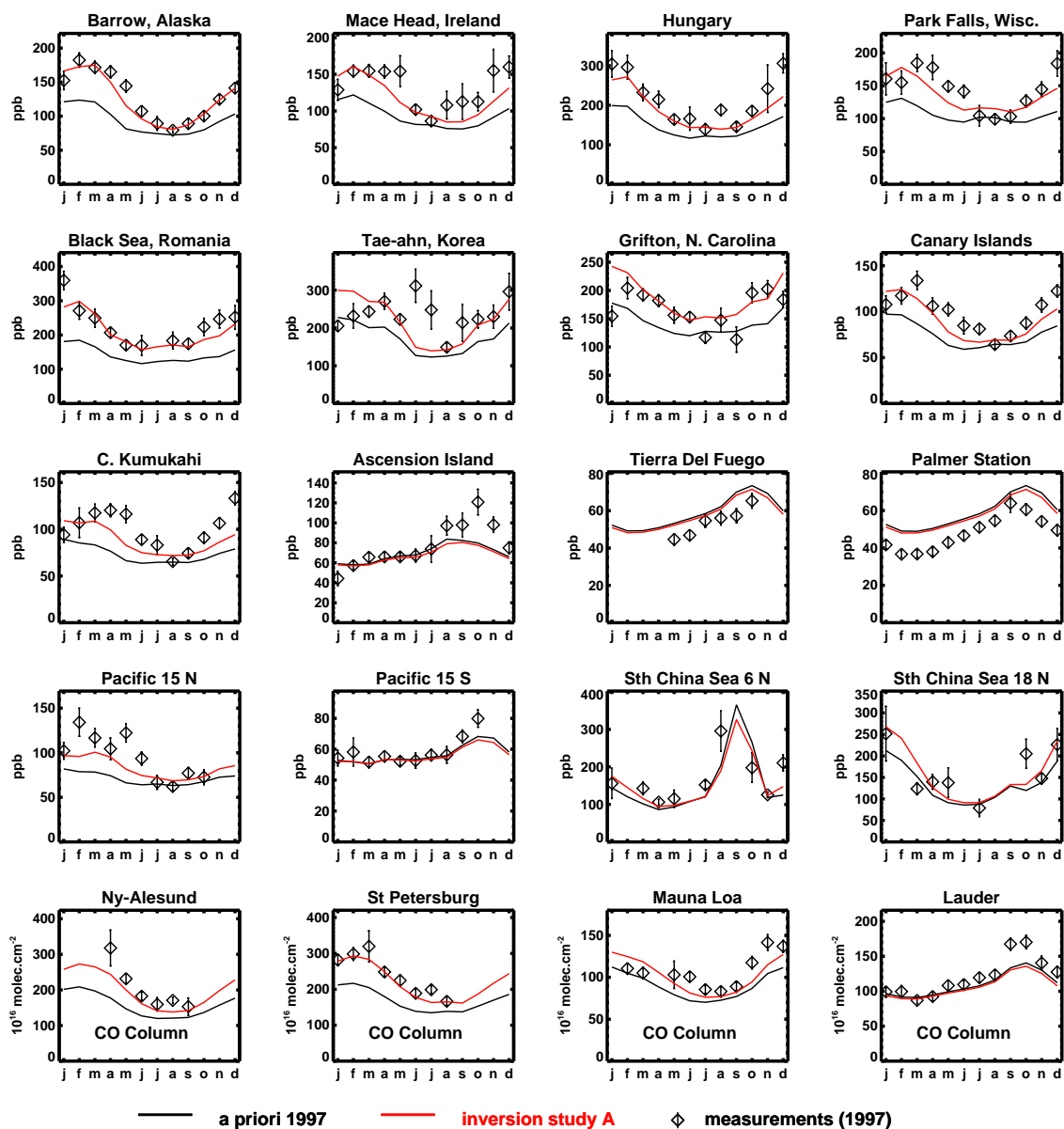


Fig. 9. Comparison between modelled and observed monthly averaged CO mixing ratios for case study A at selected CMDL and column-measuring stations.

constraint in case C has only a negligible influence on CO outside the Tropics. Model transport flaws are likely to explain most of the remaining discrepancies between observed and optimized mixing ratios. The well reproduced concentration peak observed by the shipboard cruise at 6° N from August to October 1997 (also detected by GOME, as seen on Fig. 10) is due to intense Indonesian forest fires (e.g., Hauglustaine et al., 1999; Duncan et al., 2003), which appear to be correctly represented in the 1997 emission inventory. A good agreement between optimized and observed CO columns is achieved in the Northern Hemisphere (Ny-

Alesund, St-Petersburg, Mauna Loa). However, the inversion has only a small impact on the calculated mixing ratios and columns at Southern high latitudes (Lauder, Wollongong, Cape Grim, Crozet, Tierra del Fuego, and the Antarctic stations). In this region, the model underestimates CO columns, while overestimating the surface concentrations. This feature is consistent with the underestimation of vertical gradients at these latitudes seen in the comparisons with aircraft measurements (see Sect. 6).

The inversion study A predicts an increase of the global surface emission flux of CO by 4%, whereas slight decreases

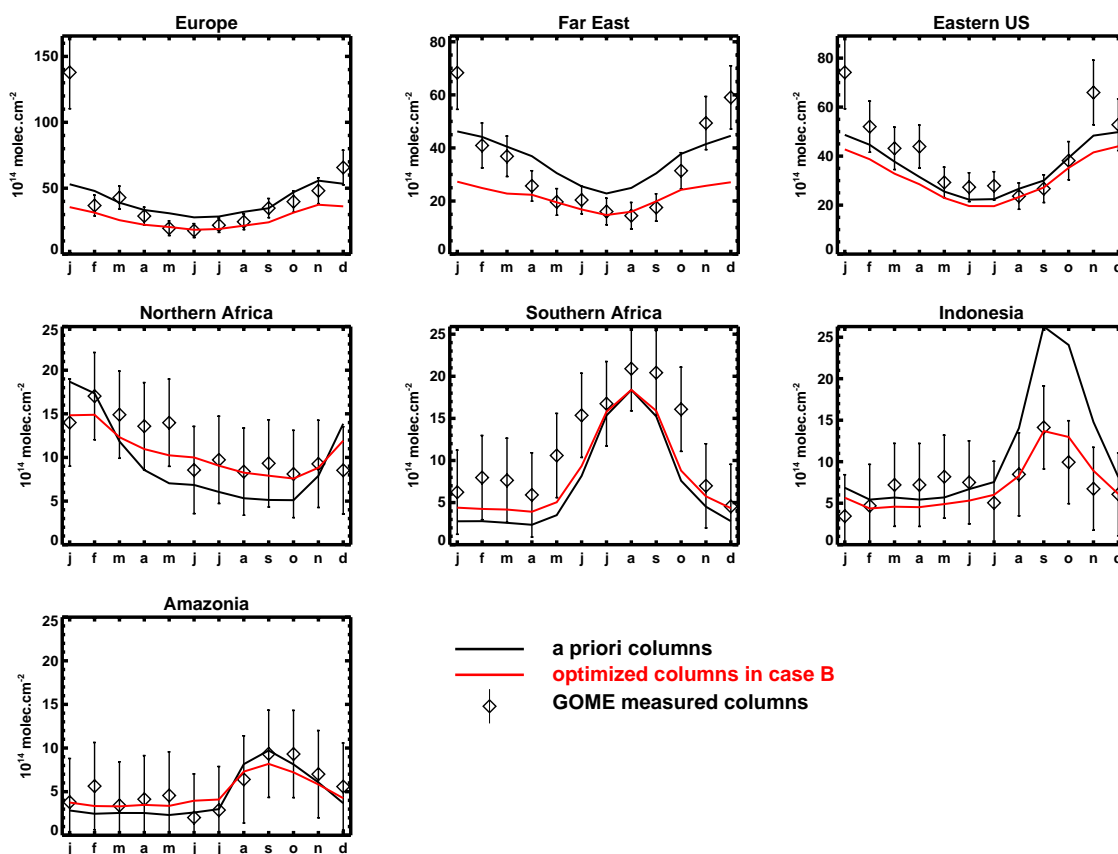


Fig. 10. A priori and optimized NO₂ modelled columns compared to observed columns averaged over the geographical areas illustrated in Fig. 11.

are found in cases B and C (2% and 5%, resp.). The photochemical production of CO by methane and NMVOCs oxidation decreases in all cases, by 1% in case A, 8% in B, and 11% in case C, as shown in Table 10. The direct sources increase is mostly due to anthropogenic emissions over industrialized regions and countries in economical transition. More precisely, the largest increases occur over N. America (48% in A, 37% in B and C), Europe (24% in A, 16% in B and C), Former Soviet Union (168% in A, 145% in B, 151% in C), South Asia (29%, 23%, 25% in A, B, C resp.), and Far East (21% in A, 14% in B, C), with respect to their prior values displayed in Table 4. The different inversions agree on a decrease of about 16% over Oceania.

The TAR recommended value for the total CO source of year 2000 amounting to 2780 Tg CO/yr (IPCC, 2001), compares very well with our inversion results, in particular the estimate in case B (2760 Tg CO/yr). Furthermore, anthropogenic emissions derived by our analysis and the estimates proposed by IPCC (2001) are generally in good agreement, e.g. over North America and Africa (their 137 against 124–134 Tg CO/yr, their 80 against 79–86 Tg CO/yr, respectively), with the exception of European anthropogenic emissions, estimated at 109 Tg CO/yr by IPCC (2001), i.e., sig-

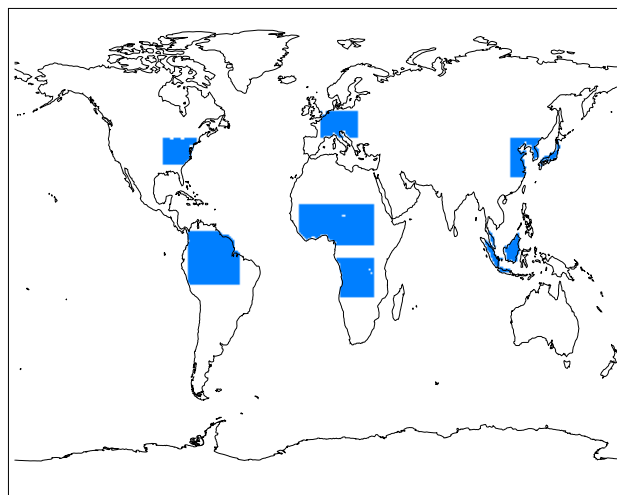


Fig. 11. Localisation of the geographical areas used in Fig. 10.

nificantly higher than our best estimates ranging between 54 and 58 Tg CO/yr.

Table 10. A priori and optimized 1997 global CO emission fluxes and deposition expressed in Tg CO.

Source category	A priori	Case A	Case B	Case B1	Case B2	Case C
Anthropogenic	571	760	730	716	721	731
Vegetation fires	409	359	356	342	407	336
Biogenic	160	142	128	149	97	127
Oceans	20	23	26	20	66	20
CH ₄ oxidation	876	870	825	829	835	790
NMVOCs oxid.	787	774	695	749	628	684
Total	2823	2928	2760	2805	2754	2688
Deposition	231	203	186	199	142	205
CO lifetime (days)	45	46.5	49.2	48.6	49.4	51.4
CH ₄ lifetime (yrs)	8.55	8.63	9.13	9.09	9.03	9.58
χ^2 (CO data)	4.43	2.58	2.25	2.41	2.17	2.20
χ^2 (NO _x data)	1.38		0.78	0.81	0.76	0.79

Table 11. A priori and optimized global 1997 NO_x emission fluxes, expressed in Tg N. Aircraft emissions are included.

Source category	A priori	Case B	Case B1	Case B2	Case C
Anthropogenic	30.9	22.8	24	21	22.5
Vegetation fires	6.9	4.4	4.9	4.1	4.4
Soils	8	12.1	11	10.9	12.1
Lightning	3	2.8	3.2	2.8	1.6
Total	48.8	42.1	43.1	38.8	40.6
Deposition	4.9	7.5	7.1	6.3	7.5

A posteriori anthropogenic emissions over South America and Africa present a more significant increase in case B, compared to the other inversion studies. For instance, African emissions increase by 12% in B, and by 3% in A, while emissions over South America decrease by 3% in A, increase by 6% in B and remain constant in C. The increase in Tropical CO emissions in case B appears to be necessary in order to compensate for the higher photochemical sink of CO caused by increased Tropical NO_x emissions, as will be discussed further below.

The biogenic emissions of CO and NMVOCs are decreased by 11–20%. The posterior isoprene emissions amount to 504 Tg/yr in case A and 454 Tg/yr in case B, while monoterpene emissions amount to 128 Tg/yr in A and 115 Tg/yr in inversion B. Biomass burning emissions of CO are decreased by 12–18% compared to their bottom-up value (Table 10). Savanna burning emissions decrease by a factor equal to 1.4 in A and 1.3 in B. Asian tropical forest burning emissions are reduced by 15–22%. On the other hand, extratropical forest burning emissions present an important increase (43% in A, C, 50% in B) which might be partly driven by the model underestimation at Tae-ahn in June–July (Fig. 9). Whereas African forest burning emissions preserve their a priori value in case study A, they increase significantly when GOME observations are considered in the inversion (55% in B, 50% in C). Note that the magnitude of the latter two sources being very small (Table 5), these large relative

changes predicted by the inversions have only a small influence on the concentrations. As will be explained in Sect. 7, little confidence should be given to the results obtained on vegetation fire emissions, since their estimated a posteriori uncertainties remain quite large.

Inversion studies B and C predict a decrease of the global annual NO_x emissions by 14–17%, as described in Table 11 and illustrated in Fig. 12. It is mostly due to pronounced anthropogenic emission decreases over the Former Soviet Union (52%), the Far East (36%), and Europe (27%). Although these changes bring the calculated NO₂ columns closer to the observations during the summer over Europe and the Far East (Figs. 10, 11), they also result in a significant underestimation in wintertime. The reasons for this poor representation of the seasonal cycle of NO₂ columns at mid-latitudes are unclear.

Whereas in case A, the higher CO anthropogenic emissions lead to a decrease in OH abundances at mid- and high latitudes, amounting to 15–25% on annual average, the NO_x decrease at mid-latitudes in cases B and C brings OH at still lower levels at these latitudes, on the order of 25–35%, as seen on Fig. 13. The resulting longer CO lifetime explains the weaker increases of CO anthropogenic emissions at mid-latitudes in cases B and C, compared to case A. This gives an example of how the chemical interplay between NO_x and CO influences the inversion results.

Table 12. A priori and optimized CO emission fluxes over different regions expressed in Tg CO/yr.

CO emissions	A priori	Case A	Case B
Europe	89.3	146.2	134.8
N. America	142.5	184.3	173.7
S. America	216.4	215.7	193.8
Africa	213.1	191.4	211.7
Far East	147.0	175.4	165.5
S. Asia	302.9	317.8	305.8

Another example is provided by the decrease in biogenic CO and VOC emissions noted in case B. This change is related to the underestimation of NO₂ columns in the a priori simulation over continental tropical regions during the wet season (Fig. 10), which lead to an increase in NO_x emissions over those regions: anthropogenic emissions over Africa increase by 19%, and the tropical soil emissions almost double, reaching 10.5 Tg N. In an attempt to further increase NO₂ abundances in the Tropics, the inversion scheme provides decreased biogenic VOC emissions, because the formation of nitrates and PAN associated with the oxidation of biogenic VOCs (in particular isoprene) is a significant sink of NO_x over source regions (Chen et al., 1998). As a result, an increase by 30% in oceanic CO emissions is also predicted, which partly compensates for these decreased biogenic emissions and for the substantial increase in OH levels in the Southern Tropics, as seen on Fig. 13. A sensitivity test, where the isoprene nitrate yield passes from 8% to 4%, has been carried out. The impact of this change is a reduction of tropical soil emissions by 10%, and an increase of the biogenic NMVOC emissions (4%), confirming the significance of the nitrate yield in the inversion.

In case C, the tropical OH concentrations are decreased, driven by the constraint on the methane lifetime. This decrease is achieved by a 47% decrease in lightning emissions, compensated by increased soil NO_x emissions (Table 11). As a consequence, the CO lifetime increases in this case (14% globally), especially over remote areas (oceans), where lightning emissions are dominant. In this case, the increase of the oceanic sources, noted in case B, is no longer necessary.

In Tables 12 and 13, we compare the prior global CO and NO_x emissions over large geographical regions with their values after optimization. The CO emissions over Europe, North America, and Far East increase by 50%, 23% and 13%, respectively, while they decrease by 10% over S. America, and remain approximately constant over Africa and S. Asia, in inversion analysis B. Note here that the results of the optimization in case A give larger values for the emissions in all regions, except for Africa. As illustrated in Fig. 10, the model overestimation of NO₂ columns over Europe, N.

Table 13. A priori and optimized NO_x emission fluxes over different regions expressed in Tg N/yr.

NO _x emissions	A priori	Case B
Europe	8.04	5.03
N. America	8.83	8.30
S. America	5.70	6.15
Africa	6.89	8.83
Far East	6.42	4.15
S. Asia	7.68	5.10

America and Far East leads to a reduction of top-down fluxes over these regions: 37%, 6%, and 35%, respectively. On the other hand, African and South American NO_x emissions are increased, driven by the large NO₂ observed columns over these regions.

Two sensitivity tests have been performed for inversion study B. The a priori errors on the control parameters are halved in the first (B1), and doubled in the second one (B2). In the first case, strong confidence is granted to the a priori information, whereas larger uncertainties are allowed in the second case. As a result, convergence is attained faster in the B1 optimization, but is slowed down in the B2 scenario. Anthropogenic sources of NO_x over Europe, Far East, Oceania, South Asia and North America, as well CO sources over Europe, North and South America, and S. Asia are found to be insensitive to the changes of errors in both experiments. The remainder of anthropogenic sources present weak sensitivity, varying between 10 and 30% compared to case B, with the exception of NO_x emissions by ships, whose value in case B (1.65 Tg N) is increased by 28% in B1 and decreased by 36% in B2 (Fig. 12). This large variability is related to the fact that GOME oceanic pixels have not been considered in the inversion (Sect. 4.2), and therefore emissions by ships are poorly constrained.

Tropical forest and savanna burning CO emissions are found to be strongly dependent on the choice of background errors. Note in particular, the increase of the small African tropical forest burning emissions, which are multiplied by 6 in case B2. As seen in Fig. 12, natural NO_x emissions as well as the photochemical CO production from the oxidation of methane are relatively stable. The weak oceanic CO source, however, is subject to a strong variability, reaching the value of 66 Tg CO/yr in case B2, while the biogenic CO and VOC emissions are decreased by 24% (Table 10). In the B2 scenario, the inversion attempts to reduce the model/data biases for CO in the Northern Hemisphere, by increasing the CO lifetime, and thus decreasing the anthropogenic NO_x emissions, as can be seen in Table 11. In addition, the overestimated CO mixing ratios at remote stations of the Southern Hemisphere (Fig. 9), especially in the wet season, entail the reduction of biogenic CO and VOC emissions, and the

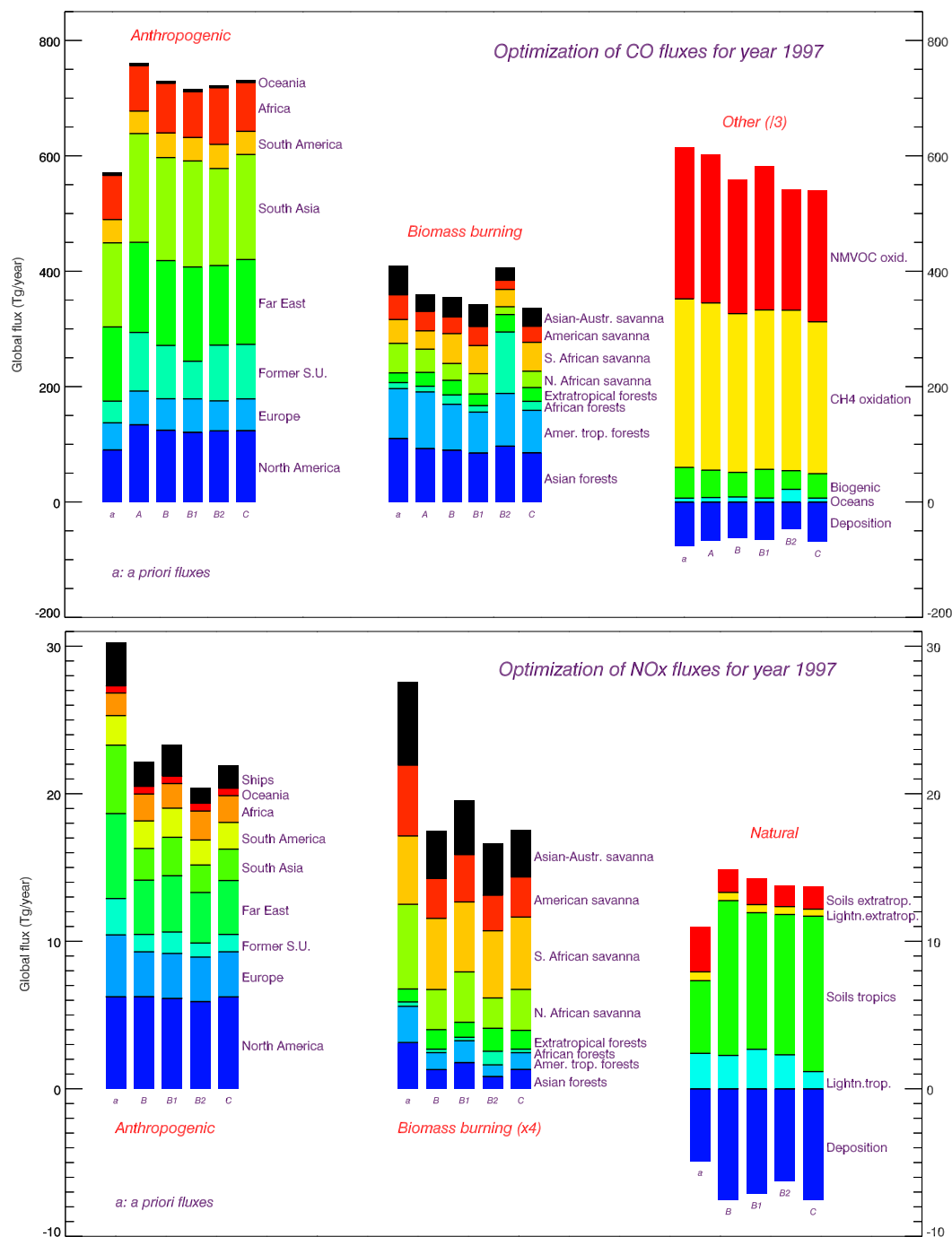


Fig. 12. Global annual CO and NO_x fluxes for the case studies presented in Table 9.

increase of oceanic emissions. As explained earlier, lower values of NMVOC biogenic emissions lead to a reduction of the sink of NO_x, and therefore, the NO_x soil emissions are also reduced in case B2, compared to case B.

6 Comparison to independent observations

The inversion studies are evaluated against independent observations obtained during the measurement campaigns described in Table 8. Despite the fact that most of these campaigns did not take place in 1997, the comparison of these measurements with the modelled CO abundances is

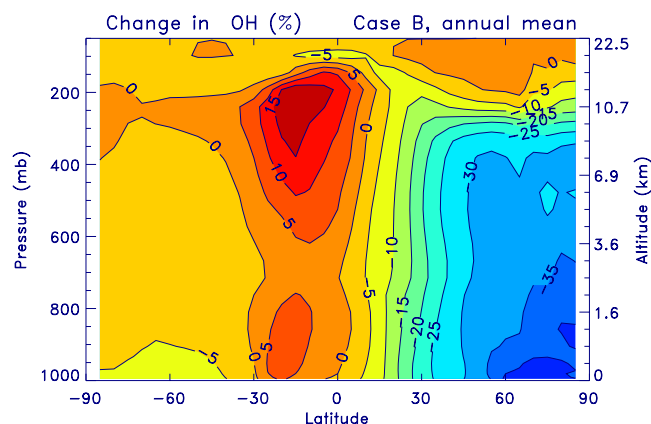


Fig. 13. Zonally and annually averaged changes in the calculated OH concentrations in case study B.

meaningful, provided that the CO interannual variability (between 1997 and the campaign year) is taken into account in the comparison, as described below in several cases.

The comparisons are displayed in Figs. 14 and 15. The ratios of the root mean square relative deviations of the optimized simulations by the corresponding a priori values are given in Table 14. Values lower than unity in this table indicate a reduction of the model/data bias after optimization. As illustrated in Table 14, for all three cases, the improvement is more significant at the high and mid-latitudes of the Northern Hemisphere, as well as in South Asia. In case A, however, the inversion fails to improve the agreement with the observations in most Tropical regions and in the Southern Hemisphere. The simultaneous optimization of CO and NO_x (cases B and C) results in a better performance of the model in all regions, compared to case A. In case C, the quality of the inversion worsens in the Tropical Pacific and in the Southern Hemisphere, where the lower OH concentrations, implied by the methane lifetime constraint, lead to higher CO mixing ratios.

The increase of the optimized mixing ratios at the northern high latitudes stems from the model underestimation in those regions (Fig. 9), as seen for different campaigns in Fig. 14. The discrepancy between optimized mixing ratios and OCTA-4 observations in boreal regions is partly due to interannual variability. For instance, a mean value of 165 ppb during March–April 1997 has been observed at Ocean Station M (Table 6), i.e. 12 ppbv below the value observed during the same period in 1994, when the OCTA-4 mission took place. In addition, as already noted, the model underestimation at high latitudes is usually larger during springtime, as seen e.g. at Point Barrow (Fig. 9).

The agreement between inversion results and observations is excellent for a number of campaigns in the northern mid-latitudes, like PEM-West-B in the North Pacific, PEM-Tropics-A and ACE-1 in North America, and SONEX over the North-Eastern Atlantic. The inversion results match very

Table 14. Ratios of the root mean square relative deviations (averaged over all campaigns and altitudes in the regions shown in Fig. 8) calculated after optimization in cases A, B and C by their corresponding values in the a priori simulation.

Regions	Case A	Case B	Case C
Boreal	0.42	0.39	0.38
N. Pacific	0.61	0.61	0.62
N. America	0.64	0.62	0.62
N.-E. Atlantic	0.72	0.72	0.71
Trop. Atlantic	1.03	0.71	0.68
S. America	1.03	0.97	0.93
Africa	1.03	0.93	0.92
S. Asia	0.76	0.76	0.78
N. Trop. Pacific	0.97	0.94	0.98
S. Trop. Pacific	0.98	0.83	1.02
S. Mid-latitudes	0.93	0.84	0.87
Austral	0.85	0.80	0.87

well the 1997 SONEX and POLINAT-2 campaigns, taking into account the small number of POLINAT measurements between 1 and 5 km over the North-East Atlantic. The optimization falls short of the observations over the United States in the SUCCESS campaign, as also observed in April–May at the CMDL stations of Park Falls (Fig. 9) and Niwot Ridge (not shown). As displayed in Fig. 14, the model fails to reproduce the observations of the OCTA campaigns over the North-East Atlantic. The large underestimation of the modelled concentrations near the surface can be partly explained by the low mixing ratios observed by CMDL and used in the inversion: their values at Mace Head during OCTA-4 (1/03–26/04 1994) were higher by 12 ppb compared to the corresponding 1997 values. Regarding the OCTA-2 mission (19/08–1/09 1993), the Canary Islands and Mace Head stations report concentrations by 26 ppb and 22 ppb higher, respectively, compared to the values used in the inversions.

Several reasons contribute to the relatively poor performance of the inversions in the Tropics and in the Southern mid-latitudes (Fig. 15). A larger number of control parameters describing Tropical CO and VOC emissions, that would potentially allow for a better performance of the inversion scheme, cannot be constrained due to the limited number of observations available over these latitudes. The relatively large differences between the biomass burning emissions predicted in the three inversions performed (Fig. 12) show the importance of chemical feedbacks in these inversions. Caution is required when interpreting the results, since, as will be discussed in the next section, the errors associated to the biomass burning emissions remain large after optimization. Note finally that the observed vertical profiles in the Southern mid-latitudes (during PEM-Tropics-B, TRACE-A and ACE-1) are not reproduced by the inversion, presumably because of transport (convection and diffusion) errors in the model.

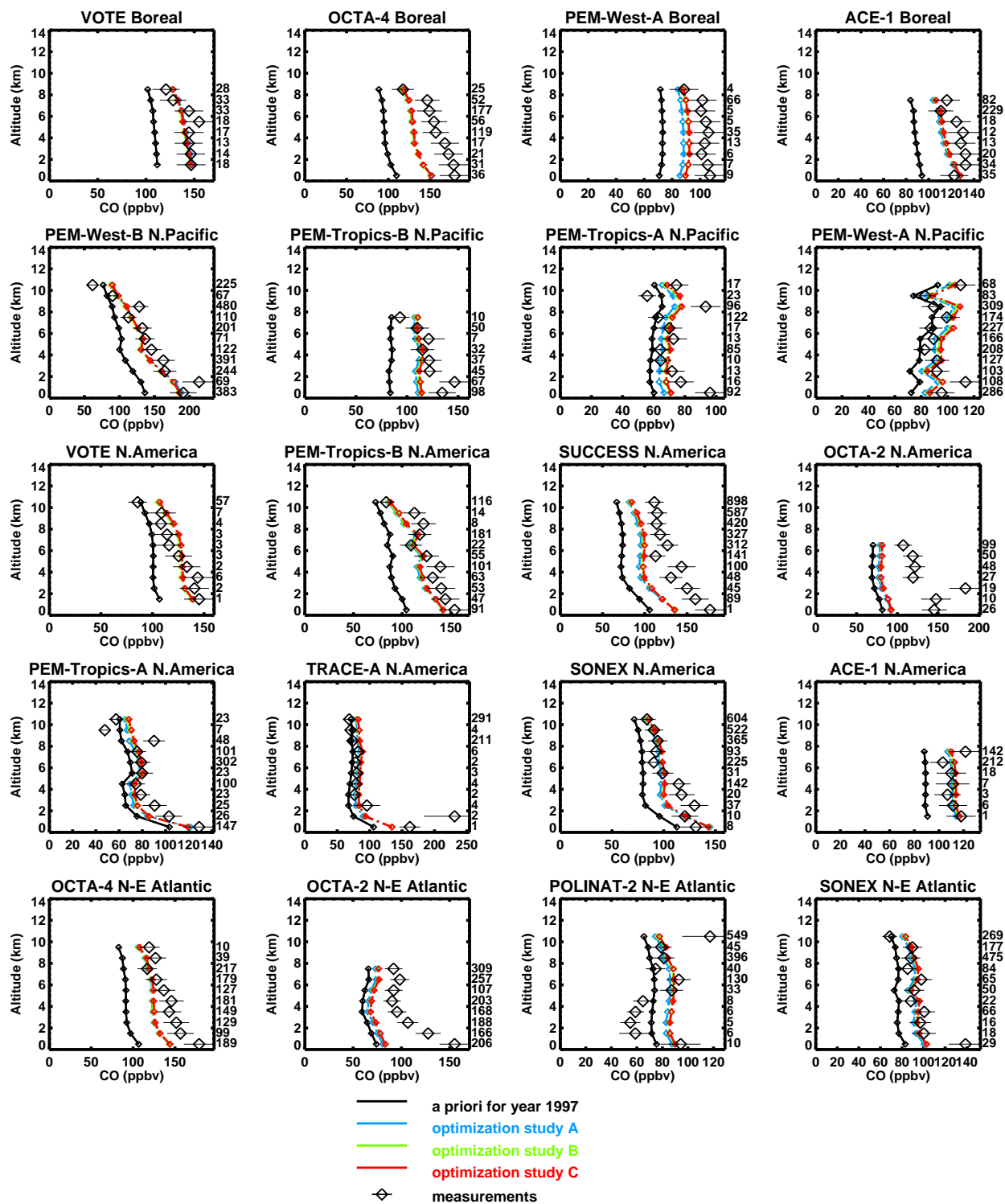


Fig. 14. Comparison of CO mixing ratios from aircraft campaign measurements at mid- and high latitudes (averaged over the regions of Fig. 8) and optimization results in case studies A (in blue), B (in green) and C (in red). Model values are extracted from the corresponding month of observations. The numbers on the right end of each plot represent the number of measurements available at the corresponding altitude.

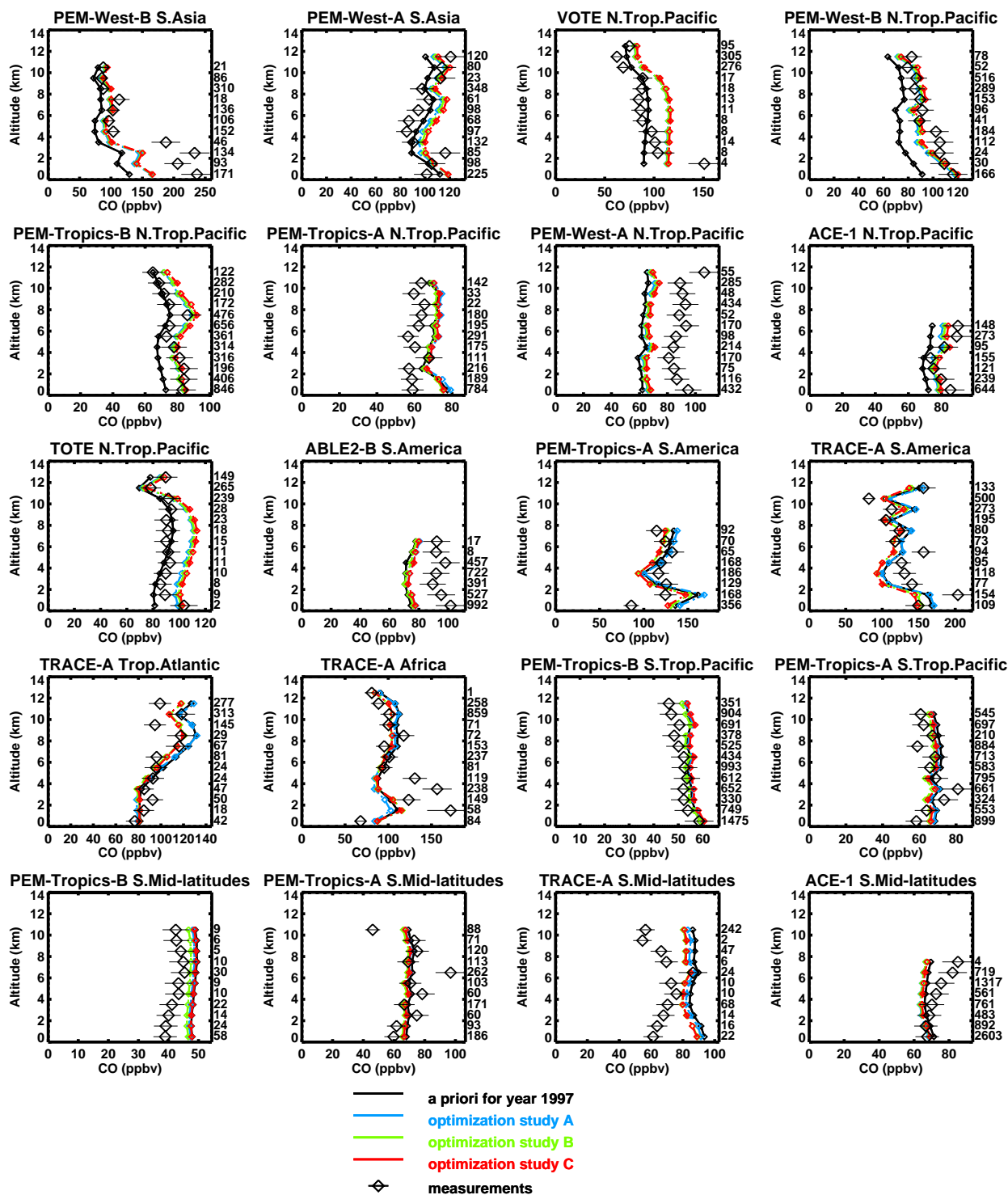


Fig. 15. As Fig. 14, for Tropical regions and the Southern Hemisphere.

7 A posteriori errors on the control parameters

The reduction of the uncertainties on the optimized fluxes is one of the goals of the inversion scheme, but also a factor

indicating its performance. A posteriori errors are sensitive to the choice of the a priori parameters and to their assumed uncertainties. For example, increasing the number of control variables, without broadening the observational datasets

Table 15. Comparison between a priori and a posteriori error estimates (expressed in %) for cases A and B. The a posteriori errors shown here are calculated by finite differences.

Control parameters		A priori errors (%)	Case study A (%)	Case study B (%)
CO anthropogenic emissions	N. America	65	22	23
	S. America	100	93	105
	Africa	100	130	105
	Europe	65	38	36
	Far East	100	34	39
	Former S.U.	100	49	52
	South Asia	100	54	57
Natural emissions	Oceania	65	58	58
	Biogenic	170	22	35
CO dep.vel.	Oceanic	170	183	166
		100	80	82
Forest fires: CO emissions	Tr. Asia	450	232	209
	Tr. America	450	293	238
	Africa	450	390	273
	Extratropical	450	475	352
Savanna fires: CO emissions	N. Africa	450	452	135
	S. Africa	450	352	194
	America	450	375	242
	Asia/Australia	450	352	245

used in the inversion, leads to reduced constraints on these parameters, and consequently, to higher uncertainties.

As pointed out in Sect. 3.3, in the linear approximation, the posterior error covariance matrix of the control variables is the inverse Hessian matrix of the cost function at its minimum. When many control variables are involved, the full error covariance matrix is very large, and its computation can be prohibitive. In this work, due to the limited number of control parameters, the Hessian matrix has been explicitly computed by applying finite differences on the adjoint model, for the inversion studies A and B. As discussed in Sect. 3.3, the validity of the linear approximation (i.e., of Eq. 16) has been verified in case A by finite difference calculations. The square root of the diagonal elements of the inverse Hessian matrix are the standard errors associated to the optimized control parameters, while the off-diagonal terms represent the correlations between pairs of parameters. A priori and a posteriori error estimates for CO-related parameters are compared in Table 15. These errors are calculated by using the values of Δf_j of Tables 4 and 5 and Eq. (2) as follows:

$$\frac{\exp(f_j + \Delta f_j)\Phi_j(x, t) - \exp(f_j)\Phi_j(x, t)}{\exp(f_j)\Phi_j(x, t)} \cdot 100\% \\ = (\exp(\Delta f_j) - 1) \cdot 100\%. \quad (21)$$

In all cases, the a posteriori errors are smaller than the a priori error estimates, except for the African anthropogenic

CO sources. Higher posterior errors are possibly related to the non-linearity of the inversion scheme, and to the fact that African emissions are not well constrained by the data in inversion study A. As shown by Talagrand (2003), non-Gaussian probability density distributions may result in posterior variances larger than their prior values.

Of all sources, the uncertainty for biogenic fluxes decreases the most, and the error reduction (ratio of the a priori by the a posteriori error) is equal to 7.7 in case A and 4.8 in case B. It is therefore expected that the optimization is not too sensitive to changes of the a priori value of this control parameter. This is confirmed by a sensitivity test carried out in case B where the biogenic source has been halved. In this case, the optimized biogenic emission flux is reduced by less than 2% compared to the value given in Table 10.

Regarding the anthropogenic sources, the largest error reductions are achieved over N. America (about 2.9) and Far East (2.9 in case A, 2.6 in case B), due to the wide coverage of the CMDL network in the northern mid-latitudes. Significant reductions are also observed over the Former Soviet Union and over South Asia. Note that the error reductions obtained in case B are generally similar to those obtained in case A. The absence of a significant error reduction for South American and African anthropogenic CO sources is explained by the limited amount of data available in the Southern Hemisphere. Nevertheless, while still being over its a priori value, the a posteriori error of the African source is lower in case B compared to case A.

Although significant error reductions are obtained for several biomass burning emission parameters, the posterior uncertainties still remain quite large. They even increase in the case of extratropical forest fires in case A. In particular, the reduction of the uncertainties associated to savanna fires emissions is more significant in case B, reaching 3.3 for N. Africa and 2.3 for S. Africa. This is explained by the strong constraints for savanna burning-related control variables, provided by the GOME NO₂ columns over Africa. The errors on the Asian (mostly Indonesian) forest fires emissions are also reduced by a factor of about two in both cases.

The error reductions are significant also for NO_x-related control parameters. The largest reductions on anthropogenic parameters occur over N. America (3.1), Europe (2.8), Far East (2.6), followed by Former S. Union (2.2), and Africa (1.9). The errors on the tropical soil emissions decrease from 170 to 30%. The NO_x biomass burning emissions are better constrained than their CO counterparts in all cases. The largest error reduction is obtained for the S. African savanna source (factor of 3). Generally speaking, the best constrained sources happen to be also the strongest (like biogenic emissions).

The off-diagonal terms of the inverse Hessian matrix can be transformed into error correlations by the formula:

$$\text{corr}(i, j) = \frac{(IH)_{ij}}{\sqrt{(IH)_{ii}(IH)_{jj}}}, \quad (22)$$

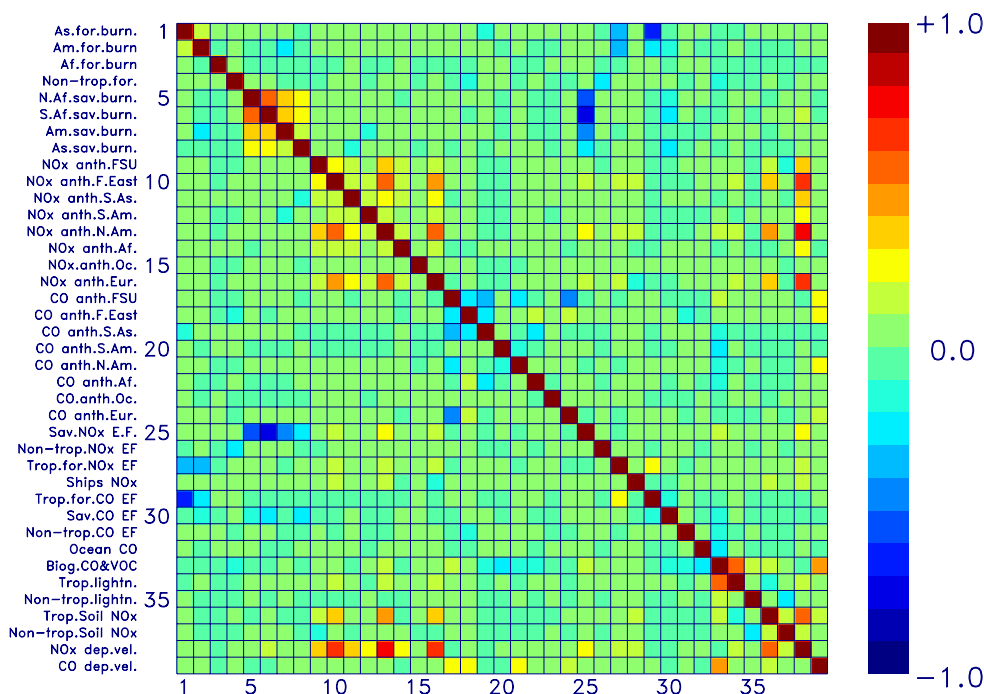


Fig. 16. Correlation matrix plot for the inversion study B.

where $(IH)_{ij}$ are elements of the inverse Hessian matrix. A small value implies little correlation, whereas a value close to 1 corresponds to a strong correlation. By definition, the correlation equals 1 for diagonal terms. For the sake of simplicity, we only examine the inversion study B.

Strong correlations occur between NO_x deposition velocity and control parameters related to NO_x emissions, like anthropogenic sources over North America (0.79) and Far East (0.64), as illustrated in the correlation matrix plot of Fig. 16. Due to this dependence, the NO_x sources become themselves intercorrelated. For instance, anthropogenic sources over Far East present positive correlations with anthropogenic sources over North America (0.53), over Europe (0.41), or the tropical soil emissions (0.36). Similarly, the CO deposition velocity parameter is correlated to other CO sources, notably the biogenic CO and VOC source (0.45) and the anthropogenic emissions over Former S. Union (0.25). Anticorrelations are introduced due to the description of biomass burning emissions by emission factors, one the one hand, and burnt biomass over large regions, on the other. For instance, the savanna burning NO_x emission factor parameter is strongly anticorrelated with savanna burning emissions over North Africa (−0.57), South Africa (−0.74), America (−0.41) and Asia (−0.28). Another source of correlation arises from the chemical coupling between CO, NO_x and NMVOCs. This concerns, however, mostly tropical sources. For example, biogenic CO and VOC sources are correlated to tropical lightning emissions (0.51). In addition, correlations occur between CO sources which, due to the long

CO lifetime, influence the same measuring stations. The strongest anticorrelations in this case are seen between anthropogenic CO sources over Europe and over Former Soviet Union (−0.47), or over South Asia and Far East (−0.28). With the exception of ship NO_x and oceanic CO emissions, whose coupling to other sources is very weak, in most cases, important correlations are found between the majority of the control variables.

The off-line iterative approximation of the inverse Hessian using the inverse BFGS and DFP update formulas (Eqs. 17 and 18) has been evaluated against the finite difference approach. As illustrated in Figs. 17 and 18, the DFP update performs better than the BFGS approximation in both cases, compared to the finite difference approach. In particular, the BFGS method produces a systematic overestimation of a posteriori errors. The error reductions computed using the DFP formula prove to be more significant compared to those calculated by finite differences in inversion A, but they are slightly underestimated in case B. The reasons for the better approximation to the inverse Hessian provided by DFP, compared to BFGS, are still unclear.

8 Comparison of the inversion results to past studies

The study of Pétron et al. (2002) applies the “tagging” inversion technique in an earlier version of the IMAGES model. It uses the monthly averaged CO concentrations observed at 39 CMDL stations during the period 1990–1996 in order to optimize 33 CO sources, including monthly emissions

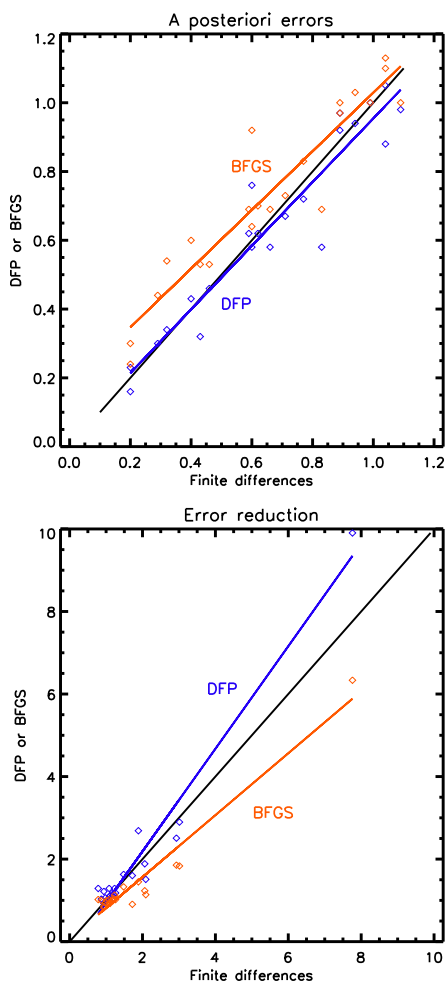


Fig. 17. Comparison between a posteriori errors calculated by finite differences and errors determined using the BFGS and DFP formulas for the inversion study A. The error reduction is given by the ratio: $(\exp(\epsilon_0) - 1) / (\exp(\epsilon) - 1)$, where ϵ_0 and ϵ are the a priori and a posteriori errors, respectively.

by technological activities, biomass burning, vegetation and oceans over large regions. Based on the EDGAR v2.0 anthropogenic emissions for 1990 (Olivier et al., 1996) and biomass burning emissions by Granier et al. (2000), the prior direct emissions amount to 1296 Tg CO/yr, or about 10% higher than in the present work, whereas the photochemical CO production is about 20% lower than the prior value displayed in Table 10. The total prior sources amount to 2669 Tg CO/yr, to be compared to 2823 Tg CO in the present study (Table 10). In the following, we compare our case study A with the second iteration analysis results of Pétron et al. (2002), i.e. those results obtained using OH fields calculated by the full chemistry version of the model using the optimized CO emissions from the first iteration.

Although the values of the posterior global emission fluxes predicted by both studies are very close (2960 against

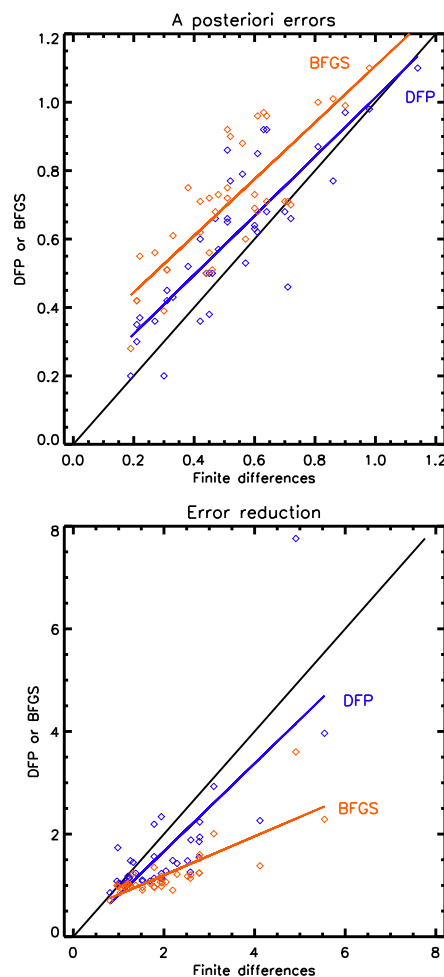


Fig. 18. As in Fig. 17, but for the inversion study C.

2928 Tg CO/yr in case A), the increase is more important in Pétron et al. (2002). It is mostly due to a 73% increase of the annual flux over Asia, whose posterior value of 686 Tg CO/yr is substantially higher than our estimate of 539 Tg CO/yr (case A), which is only 12% higher than our prior Asian flux of 479 Tg CO. Part of this disagreement can be explained the inclusion of the South China sea shipboard measurements. Moreover, whereas Asian anthropogenic emissions are described by only one control parameter in Pétron et al. (2002), in our inversion scheme, Asia is subdivided into smaller geographical areas. As a result, the large underestimation of the high latitude CO mixing ratios in the a priori simulation leads to a large increase of anthropogenic emissions over the Former Soviet Union (and other high latitude regions) in our study, instead of a global emission increase over Asia as in Pétron et al. (2002). In fact, South Asian emissions, whose influence on the high latitudes is negligible, increase by only 29% in our study.

The two studies predict reasonably similar total emissions over Europe and North America: 160 and 197 Tg CO/yr in

Pétron et al. (2002), and 146 and 184 Tg CO/yr, respectively, in inversion study A.

Bergamaschi et al. (2000b) apply a Bayesian inverse modelling technique to optimize the global annual CO emissions from nine separate CO source categories, while the seasonality of all sources remains fixed. The observations are provided by 31 CMDL sites in the 1993–1995 period and complemented by isotope data. Biogenic CO emissions are not considered. Although the total prior source (2860 Tg CO/yr) is very close to our value of 2823 Tg CO, there are large discrepancies regarding individual emission categories. For instance, the a priori 850 Tg CO/yr emitted by vegetation fires represent almost twice our estimate for this source (409 Tg CO/yr). In contrast, the CO production from the oxidation of NMVOCs (560 Tg CO/yr) in Bergamaschi et al. (2000b) is about 30% lower than in our a priori simulation (Table 10). Prior anthropogenic emissions in the two studies compare very well, 600 against 571 Tg CO/yr.

The optimized global budget ranges from 2842 to 2958 Tg CO/yr, in excellent agreement with our inversion results (Table 10). In particular, depending on the emission scenario, top-down anthropogenic source strengths are increased by 5–25% (28–33% increase in our work), and biomass burning emissions are decreased by 5–22% (12% in our study). The a posteriori emissions by NMVOCs oxidation range between 490 and 748 Tg CO/yr in Bergamaschi et al. (2000b), to be compared with our estimates of 774 Tg CO/yr. An excellent agreement is also obtained between the two studies regarding the total CO source in the Northern Hemisphere (1840–1932 Tg CO/yr in Bergamaschi et al. (2000b) vs. 1755–1932 Tg CO/yr in our study) and in the Southern Hemisphere (935–1077 vs. 934–996 Tg CO/yr). On the other hand, the dry deposition sink calculated in Bergamaschi et al. (2000b) (ca. 288 Tg CO/yr) is larger than the values displayed in Table 10 (186–205 Tg CO/yr).

Based on the additional constraints provided by the use of isotopic measurements, Bergamaschi et al. (2000b) estimated the total production of CO from the oxidation of methane to 747–817 Tg CO/yr, depending on the emission scenario, i.e., significantly less than in our inversion study A, but in good agreement with cases B and C. The average CO yield of 86% in the oxidation of methane, suggested by Bergamaschi et al. (2000b), is to be compared with our yield estimated at 92.5%.

Our results might be further compared with the inversion studies of Kasibhatla et al. (2002) and Arellano et al. (2004), which both used the GEOS-CHEM global CTM and a priori emissions based on EDGAR v2.0 (Olivier et al., 1996), in order to quantify the CO sources from different emission categories and geographical regions. In Kasibhatla et al. (2002), the model predictions are compared to CMDL monthly mean concentrations for 1994 from 38 sites, while the CO mixing ratios retrieved from the MOPITT instrument between April and December 2000 are used in Arellano et al. (2004).

The global a posteriori source in Kasibhatla et al. (2002) amounts to 2846 Tg CO/yr, out of which 780–860 Tg CO/yr

is provided by anthropogenic sources. These numbers are in good agreement with our estimates, since the chemical production of CO from the oxidation of anthropogenic NMVOCs is included as a direct anthropogenic source in Kasibhatla et al. (2002). The optimized global CO burden (397 Tg CO) is about 10% higher than in our studies: 366 in A, B, and 371 Tg CO in case C. The global CO lifetime is estimated at 1.7 months by Kasibhatla et al. (2002), in excellent agreement with the value predicted in our inversion analysis C. In addition, the CO production from CH₄ oxidation is estimated at 949 Tg CO/yr, i.e., 8–17% higher than our values, and the average optimized yield to 0.95, slightly higher than our estimate.

The total optimized anthropogenic source is estimated at 774–963 Tg CO/yr by Arellano et al. (2004). As in Kasibhatla et al. (2002), this source comprises CO chemically produced from anthropogenic NMVOCs. Large discrepancies are found for anthropogenic sources over Asia (405–466 in Arellano et al., 2004, vs. 320–345 Tg CO/yr in our study) and over North America (54–88 vs. 124–134 Tg CO/yr), as well as for biomass burning emissions (486–633 Tg CO/yr in Arellano et al., 2004 vs. 336–359 Tg CO/yr in our study). Their estimated total source of CO, 2363–2450 Tg CO/yr, is significantly lower than in our study. This disagreement can be attributed to the uniform 20% reduction of the prescribed OH fields used in the calculations in Arellano et al. (2004), which implies a reduction of global CO source magnitudes.

The inversion analysis conducted by Palmer et al. (2003) focuses on Asian CO emissions. The GEOS-CHEM global CTM, driven by the Streets et al. (2003) and Heald et al. (2003) bottom-up emission inventories, is used in order to minimize the bias between model predictions and aircraft CO observations obtained during the TRACE-P mission in March–April 2001. In this study, the top-down anthropogenic emissions over Far East (China, Japan and Korea), amounting to 185–199 Tg CO/yr, are by about 13% higher than our values ranging from 165 in case B to 175 Tg CO/yr in case A. Since Palmer et al. (2003) considers the production of CO from the oxidation of anthropogenic and biomass burning NMVOCs as direct CO sources (anthropogenic sources are increased by about 20%, biofuel and biomass burning by 10%), a very good agreement can be concluded between the two studies. The best estimate of their total top-down CO source is 2353 Tg CO/yr, much less than our estimates. This discrepancy can be attributed to the CO source from the rest of the world, which is very poorly constrained by the TRACE-P data.

Next, we evaluate our a posteriori NO_x emissions against the results of Martin et al. (2003a). In this study, a top-down NO_x emission inventory has been constructed by inverting GOME tropospheric NO₂ columns for the period September 1996–August 1997 with the GEOS-CHEM model. A priori estimates are provided by the EDGAR 3.0 global inventory (Olivier and Berdowski, 2001). According to this study, the posterior global annual surface NO_x emissions amount

to 37.7 Tg N/yr. As seen in Table 11, the global magnitudes derived by our inversion scheme are 38.7 and 38.4 Tg N/yr in cases B and C, respectively, when lightning and aircraft emissions are not accounted for. Although the global emissions are therefore in excellent agreement, the top-down estimates differ significantly at the regional scale. For instance, the surface NO_x emissions over South America, Africa and South Asia, estimated at 3.85, 6.27, and 3 Tg N/yr by Martin et al. (2003a), are significantly lower than our values of 6.1, 8.8, and 5.1 Tg N/yr, respectively (Table 13).

Over Europe and the Far East, however, our optimized values of 5 Tg N/yr and 4.1 Tg N/yr are in better agreement with their estimates of 5.9 and 5.3 Tg N/yr. The overestimation of our NO_x emissions in the Tropics and in the Southern Hemisphere, is mainly due to our large soil emissions, increasing from 8 Tg N/yr in the a priori to about 12 Tg N/yr. As illustrated in Fig. 12, this increase concerns tropical soil emissions, which almost double in the a posteriori.

This disagreement between our results and those of Martin et al. (2003a) might be partly due to the different retrieval approaches used by Richter et al. (2003) and Martin et al. (2003a) to derive the tropospheric NO₂ columns. In the former study, the air mass factors are based on the MOZART tropospheric NO₂ profiles, and a simplified treatment of the effects of aerosols is used (only maritime aerosols are taken into account). In the latter, the NO₂ retrievals use shape factors from the GEOS-CHEM model, as well as a comprehensive model for the effects of aerosols. However, the discrepancies between the two studies are probably mostly due to the differences between GEOS-CHEM and the IMAGES model. For example, the isoprene nitrate yield used in Martin et al. (2003a) (4%) is twice lower than in our study. A sensitivity test conducted using this reduced nitrate yield in IMAGES resulted, as expected, in lower NO_x soil emissions (by 10%). Furthermore, it is worth noting that the prior sources for lightning and soils used by Martin et al. (2003a), 6.2 and 5.1 Tg N/yr, respectively, are quite different from our prior values (3 and 8 Tg N/yr, respectively).

Van der Werf et al. (2004) estimated the yearly emission anomalies between 1997 and 2001, based on the assumption that the CO concentration anomalies recorded by the CMDL network over that period can be attributed to interannual variability of vegetation fires. Although not strictly comparable to our results, the regional carbon emissions for 1997 derived by combining these emission anomalies with the bottom-up 1997–2001 inventory determined from satellite fire counts and a biogeochemical model (Van der Werf et al., 2003) appear to be almost systematically higher than both our prior and optimized carbon emissions, especially over Africa (factor of three) and to some extent over Asia and Latin America (factor of 1.7). This is mostly a consequence of the higher bottom-up emissions of Van der Werf et al. (2003), compared to those of (Olivier et al., 2003). The reasons for these large differences between the bottom-up inventories are unclear. The fact that biomass burning emissions are poorly

constrained by the observations used in this study might explain the relatively small emission updates after optimization. It is worth noting, however, that inversion B2, with its looser prior constraint, shows an 8-fold increase of African forest fires emissions, bringing the posterior African emissions somewhat closer to the Van der Werf et al. (2004) estimate.

9 Conclusions

We have developed and presented an inverse modelling framework based on the adjoint of the three dimensional tropospheric model IMAGES. It has been used to optimize the global annual CO and NO_x emissions over large continental regions and for different source categories, constrained by ground-based CO measurements and NO₂ tropospheric columns retrieved by a satellite instrument. Its practicability is demonstrated by the fact that one optimization run requires a reasonably long time (a few days, 8 CPUs) using affordable computer resources. Note that for more comprehensive CTMs using much shorter time steps than the IMAGES model, however, such a framework would probably be computationally too demanding for most current computer systems. The main distinctive feature of the proposed inversion scheme is the simultaneous optimization of the sources of CO and NO_x, accounting for the chemical response of the CO-OH-NO_x-NMVOC system to emission changes. As a result, observations of one of these species can benefit the optimization of the other species, since the ozone precursors are closely interrelated through the chemistry of OH. However, the interpretation of the inversion results is not always straightforward, since the optimized emissions of one compound do not depend uniquely on the observations used to constrain this compound, but also on other species through chemical feedbacks. Therefore, the reliability of the optimized emission estimates can be assessed only if we are able to identify the chemical feedbacks influencing the results.

Three inversion analyses are proposed in this work. In case study A, we invert for CO emissions using only ground-based CO measurements. In case B, ground-based CO and GOME measurements are used as constraints for improving CO and NO_x emissions, whereas in case C an additional constraint on the global methane lifetime is used to bring its value close to the TAR recommended value (IPCC, 2001) of 9.6 years. The inversion scheme performs reasonably well in all cases, as shown by the comparison between prior and posterior mixing ratios at NOAA/CMDL stations. The improvement for CO is more significant in the northern high and mid-latitudes, whereas the inversion has small impact on the CO mixing ratios at southern high latitudes. Furthermore, the optimization brings the NO₂ columns much closer to the GOME observations over all geographical regions.

The top-down global annual CO flux is estimated at 2928, 2760, and 2688 Tg CO/yr in inversions A, B, and C,

respectively. Note the decrease in cases B and C compared to the a priori, related to the lower OH abundances predicted in these simulations in most of the Northern Hemisphere. Direct CO emissions rise by 5–10%, due to an increase of anthropogenic emissions by about 30% with respect to their prior value. The largest increases occur over the Former Soviet Union, North America, South Asia and Europe. The biomass burning source, however, is reduced in all cases. The tropospheric methane lifetime is adjusted from 8.55 years in the a priori to 9.13 years in inversion B, and to 9.58 years when the methane lifetime is also constrained. The global annual NO_x flux is estimated at 42.1 Tg N/yr, out of which 22.8 Tg N/yr are due to the anthropogenic source. When the background errors of inversion B are halved or doubled, the inversion results show little sensitivity to these changes, except for the weak oceanic source, and for vegetation burning CO emissions. Evaluation of the inversion studies against independent airborne observations shows that among the three optimization studies, case B (i.e., the simultaneous optimization of CO and NO_x), results in a better performance in all regions. Although the improvement in the Tropics and the Southern Hemisphere is generally not very significant, this simulation is found to give more robust results in these regions, compared to the A and C analyses.

The a posteriori errors on the control variables are smaller than the a priori error estimates in almost all cases. As expected due to the wide coverage of the CMDL network, significant error reductions are achieved for CO anthropogenic sources over North America, Far East, Former Soviet Union, and South Asia. On the contrary, African and South American anthropogenic emissions are very poorly constrained. The uncertainties on biomass burning emission parameters, are only slightly decreased in case A. Because of the constraints provided by the observed NO₂ columns, these parameters are better constrained in case B, and their errors are reduced by a factor of about 2. Significant error reductions are also achieved for NO_x-related control parameters. As should be expected, important correlations are found between most control parameters.

Comparison of our results to previous inverse modelling studies is very encouraging. The inversion of CO emissions performed by Bergamaschi et al. (2000a,b), Pétron et al. (2002), Kasibhatla et al. (2002), Arellano et al. (2004) and Palmer et al. (2003), although not strictly comparable to case B, compare quite well to our results. Furthermore, the results of Martin et al. (2003a) are in good agreement with our global NO_x surface emissions, even though large discrepancies are found concerning regional scale emissions.

The simultaneous inversion of emissions of chemically related compounds is a quite promising research topic. Performing the optimization of fluxes on a shorter (e.g., monthly) basis or applying pixel-based inversions are some of the issues whose investigation lies ahead. It is understood that data from new satellite instruments, that will provide supplementary constraints on the global CO and NO_x bud-

gets, will be highly valuable for further progress of inverse modelling studies.

Acknowledgements. The authors would like to thank A. Richter for providing the GOME NO₂ data, as well as B. Barret, M. Makarova and N. Jones for providing their FTIR CO data. This work was supported by the European Commission under the POET (contract no. EVK2-1999-00011), the EVERGREEN (contract no. EVG1-CT-2002-00079) projects and the PRODEX programme of the ESA, funded by the Belgian Federal Science Policy Office.

Edited by: M. G. Lawrence

References

- Andreae, M. O. and Merlet, P.: Emission of trace gases and aerosols from biomass burning, *Global Biogeochem. Cycles*, 15, 955–966, 2001.
- Atkinson, R.: Gas-Phase tropospheric chemistry of organic compounds, *J. Phys. Chem. Ref. Data*, Monograph No. 2, 1994.
- Atkinson, R., Baulch, D. L., Cox, R. A., Hampson, R. F., Kerr, Jr., J. A., Rossi, M. J. and Troe, J.: Evaluated Kinetic and Photochemical Data for Atmospheric Chemistry, IUPAC Subcommittee on gas kinetic data evaluation for atmospheric chemistry, *J. Phys. Chem. Ref. Data*, 28, 191–393, 1999.
- Arellano, A. F., Kasibhatla, P. S., Giglio, L., Van der Werf, G. R., and Randerson, J. T.: Top-down estimates of global CO sources using MOPITT measurements, *Geophys. Res. Lett.*, 31, L01104, doi:10.1029/2002GL015609, 2004.
- Barret, B., De Mazière, M., and Mahieu, E.: Ground-based FTIR measurements of CO from the Jungfraujoch: characterisation and comparison with in situ surface and MOPITT data, *Atmos. Chem. Phys.*, 3, 4857–4878, 2003.
- Baughcum, S. L., Henderson, S. C., Tritz T. G., and Pickett D. C.: Scheduled Civil Aircraft Emission Inventories for 1992: Database Development and Analysis, NASA-CR-4700, National Aeronautics and Space Administration, Langley Research Center, Hampton, VA, USA, 196 pp., 1996.
- Bergamaschi, P., Hein, R., Heimann, M., and Crutzen, P. J.: Inverse modeling of the global CO cycle, 1. Inversion of CO mixing ratios, *J. Geophys. Res.*, 105, 1909–1927, 2000a.
- Bergamaschi, P., Hein, R., Brenninkmeijer, C., and Crutzen, P. J.: Inverse modeling of the global CO cycle, 2. Inversion of ¹³C/¹²C and ¹⁸O/¹⁶O isotope ratios, *J. Geophys. Res.*, 105, 1929–1945, 2000b.
- Butler, T. M., Simmonds, I., and Rayner P. J.: Mass balance inverse modelling of methane in the 1990s using a chemistry transport model, *Atmos. Chem. Phys.*, 4, 2561–2580, 2004, **SRef-ID: 1680-7324/acp/2004-4-2561**.
- Chen, X., Hulbert, D., and Shepson, P. B.: Measurement of the organic nitrate yield from OH reaction with isoprene, *J. Geophys. Res.*, 103, 25 563–25 568, 1998.
- Ciais, P., Tans, P. P., White, J. W. C., Trolier, M., Francey, R. J., Berry, J. A., Randall, D. R., Sellers, P. J., Collatz, J. G., and Schimel, D. S.: Partitioning of ocean and land uptake of CO₂ as inferred by δ¹³C measurements from the NOAA Climate Monitoring and Diagnostics Laboratory Global Air Sampling Network, *J. Geophys. Res.*, 100, 5051–5070, 1995.

- Costen, R. C., Tennille, G. M., and Levine, J. S.: Cloud pumping in a one-dimensional model, *J. Geophys. Res.*, 93, 15 941–15 944, 1988.
- DeMore, W. B., Sander, S. P., Golden, D. M., Hampson, R. F., Kurylo, M. J., Howard, C. J., Ravishankara, A. R., Kolb, C. E., and Molina, M. J.: Chemical Kinetics and Photochemical Data for Use in Stratospheric Modeling, Evaluation number 12, NASA panel for data evaluation, JPL Publication 97-4, Jet Propulsion Laboratory, Pasadena, 1997.
- Dentener, F. J. and Crutzen, P. J.: Reaction of N₂O₅ on tropospheric aerosols: impact on the global distributions of NO_x, O₃, and OH, *J. Geophys. Res.*, 98, 7149–7163, 1993.
- Duncan, B. N., Bey, I., Chin, M., Mickley, L. J., Fairlie, T. D., Martin, R. V., and Matsueda, H.: Indonesian wildfires of 1997: Impact on tropospheric chemistry, *J. Geophys. Res.*, 108, doi:10.1029/2002JD003195, 2003.
- Elbern, H., Schmidt, H., Talagrand, O., and Ebel, A.: 4D-variational data assimilation with an adjoint air quality model for emission analysis, *Environ. Model. & Software*, 15, 539–548, 2000.
- Elbern, H. and Schmidt, H.: Ozone episode analysis by four-dimensional variational chemical data assimilation, *J. Geophys. Res.*, 106, 3569–3590, 2001.
- Emmons, L. K., Hauglustaine, D. A., Müller, J.-F., Carroll, M. A., Brasseur, G. P., Brunner, D., Staehelin, J., Thouret, V., and Marengo, A.: Data composites of tropospheric ozone and its precursors from aircraft measurements, *J. Geophys. Res.*, 105, 20 497–20 538, 2000.
- Enting, I. G.: Green's function values of tracer inversion, in: Inverse methods in Global Biogeochemical Cycles, *Geophysical Monograph*, 114, 2000.
- Enting, I. G. and Mansbridge J. V.: Seasonal sources and sinks of atmospheric CO₂, *Direct inversion of filtered data*, *Tellus*, 41B, 111–126, 1989.
- Enting, I. G., Trudinger, C. M., and Francey, R. J.: A synthesis inversion of the concentration and δ¹³C of atmospheric CO₂, *Tellus*, 47B, 35–52, 1995.
- Erickson, D. J.: Ocean to atmosphere carbon monoxide flux: global inventory and climate implications, *Global Biogeochem. Cycles*, 3, 305–314, 1989.
- Errera, Q. and Fonteyn D.: Four-dimensional variational chemical assimilation of CRISTA atmospheric measurements, *J. Geophys. Res.*, 106, 12 253–12 265, 2001.
- Fan, S., Gloor, M., Mahlman, J., Pacala, S., Sarmiento, J., Takahashi, T., and Tans, P.: Atmospheric and oceanic CO₂ data and models imply a large terrestrial carbon sink in North America, *Science*, 282, 442–446, 1998.
- Friedl, R. R.: Atmospheric effects of subsonic aircraft: interim assessment report of the advanced subsonic technology program, NASA Reference Publication 1400, March 1997.
- Giering, R.: Tangent linear and adjoint model compiler, Users Manual 1.4, http://www.autodiff.com/tamc/tamc_manual.ps.gz
- Giering, R.: Tangent linear and adjoint biogeochemical models, in: Inverse methods in Global Biogeochemical Cycles, *Geophysical Monograph*, 114, 2000.
- Giering, R. and Kaminski, T.: Recipes for adjoint code construction, *ACM Trans. On Math. Software*, 24, 437–474, 1998.
- Gilbert, J.-C. and Lemaréchal, C.: Some numerical experiments with variable storage quasi-Newton algorithms, *Math. Programming*, 45, 407–435, 1989.
- Granier, C., Müller, J.-F., and Brasseur, G. P.: The impact of biomass burning on the global budget of ozone and ozone precursors, in: *Biomass Burning and Its Inter-Relationships With the Climate System*, edited by: Innes, J. L., Beniston, M., and Verstracke, M. M., pp. 69–85, Kluwer Acad., Norwell Mass., 2000.
- Guenther, A., Hewitt, C. N., Erickson, D., Fall, R., Geron, C., Graedel, T., Harley, P., Klinger, L., Lerdau, M., McKay, W. A., Pierce, T., Scholes, B., Steinbrecher, R., Tallamraju, R., Taylor, J., and Zimmerman, P.: A global model of natural volatile organic compound emissions, *J. Geophys. Res.*, 100, 8873–8892, 1995.
- Hao, W. M. and Liu, M. H.: Spatial and temporal distribution of tropical biomass burning, *Global Biogeochem. Cycles*, 8, 495–503, 1994.
- Hauglustaine, D. A., Brasseur, G. P., and Levine, J. S.: A sensitivity simulation of tropospheric ozone changes due to the 1997 Indonesian fire emissions, *Geophys. Res. Lett.*, 26, 3305–3308, 1999.
- Heald, C. L., Jacob, D. J., Palmer, P. I., Evans, M. J., Sachse, G. W., Singh, H. B., and Blake, D. R.: Biomass burning emission inventory with daily resolution: Application to aircraft observations of Asian outflow, *J. Geophys. Res.*, 108(D21), 8811, doi:10.1029/2002JD003082, 2003.
- Heland, J., Schlager, H., Richter, A., and Burrows, J. P.: First comparison of tropospheric NO₂ column densities from GOME measurements and in situ aircraft profile measurements, *Geophys. Res. Lett.*, 29(20), 1983, doi:10.1029/2002GL015528, 2002.
- Hesstvedt, E., Hov, O., and Isaksen, I. S. A.: Quasi-steady state approximation in air pollution modeling: Comparison of two numerical schemes for oxidant prediction, *Int. J. Chem. Kinet.*, 10, 944–971, 1978.
- Horowitz, L. W., Walters, S., Mauzerall, D. L., Emmons, L. K., Rasch, P. J., Granier, C., Tie, X., Lamarque, J.-F., Schultz, M. G., Tyndall, G. S., Orlando, J. J., and Brasseur, G. P.: A global simulation of tropospheric ozone and related tracers: description and evaluation of Mozart, version 2, 108(D24), 4784, doi:10.1029/2002JD002853, 2003.
- Houweling, S., Kaminski, T., Dentener, F., Lelieveld, J., and Heimann, M.: Inverse modelling of methane sources and sinks using the adjoint of a global transport model, *J. Geophys. Res.*, 104, 26 137–26 160, 1999.
- IPCC, *Climate Change 2001: The scientific basis* (contribution of Working Group I to the Third Assessment Report of the Intergovernmental Panel on Climate Change), edited by: Houghton, J. T., Ding, Y., Griggs, D. J., et al., Cambridge University Press, Cambridge UK, 2001.
- Jacob, D. J.: Heterogeneous Chemistry and Tropospheric Ozone, *Atmos. Environ.*, 34, 2131–2159, 2000.
- Jacob, D. J., Field, B. D., Jin, E. M., Bey, I., Li, Q., Logan, J. A., Yantosca, R. M., and Singh, H. B.: Atmospheric budget of acetone, *J. Geophys. Res.*, 107, doi:10.1029/2001JD000694, 2002.
- Jones, B. N., Rinsland, C. P., Liley, J. B., and Rosen, J.: Correlation of aerosol and carbon monoxide at 45° S: evidence of biomass burning emissions, *Geophys. Phys. Lett.*, 28, 709–712, 2001.
- Kaminski, T., Heimann, M., and Giering, R.: A coarse grid three-dimensional global inverse model of the atmospheric transport 1. Adjoint model and Jacobian matrix, *J. Geophys. Res.*, 104, 18 535–18 553, 1999.

- Kanakidou, M., Dentener, F. J., Brasseur, G. P., Collins, W. J., Bernsten, T. K., Hauglustaine, D. A., Houweling, S., Isaksen, I., Krol, M., Law, K. S., Lawrence, M. G., Müller, J.-F., Plantevin, R. H., Poisson, N., Roelofs, G. J., Wang, Y., and Wauben, W. M. F.: 3-D global simulations of tropospheric chemistry with focus on ozone distributions, Results of the GIM/IGAC inter-comparison 1997 exercise, European Commission, Energy, Environment and Sustainable Development, EUR 18842, 1998.
- Kasibhatla, P., Arellano, A., Logan, J. A., Palmer, P. I., and Novelli, P.: Top-down estimate of a large source of atmospheric carbon monoxide associated with fuel combustion in Asia, *Geophys. Res. Lett.*, 29(19), 1900, doi:10.1029/2002GL015581, 2002.
- Krol, M. and Lelieveld, J.: Can the variability of tropospheric OH be deduced from measurements of 1,1,1-trichloroethane (methyl chloroform)?, *J. Geophys. Res.*, 108, doi:10.1029/2002JD002423, 2003.
- Lauer, A., Dameris, M., Richter, A., and Burrows, J. P.: Tropospheric NO₂ columns: a comparison between model and retrieved data from GOME measurements, *Atmos. Chem. Phys.*, 2, 67–78, 2002, **SRef-ID: 1680-7324/acp/2002-2-67**.
- Law, K., Plantevin, P. H., Thouret, V., Marenco, A., Asman, W. A. H., Lawrence, M., Crutzen, P., Müller, J.-F., Hauglustaine, D., and Kanakidou, M.: Comparison between global chemistry transport model results and measurement of ozone and water vapour by Airbus In-service Aircraft (MOZAIC) Data, *J. Geophys. Res.*, 105, 1503–1525, 2000.
- Madronich, S. and Flocke, S.: The role of solar radiation in atmospheric chemistry, in: *Handbook of Environmental Chemistry*, edited by: Boule, P., Springer Verlag, Heidelberg, 1–26, 1998.
- Makarova, M. V., Poberovski, A. V., Gusev, I. K., Osipov, S. I., and Grassl, H.: Ground-based spectroscopic measurements of atmospheric trace gases, Proceedings of the International Radiation Symposium, St. Petersburg, Russia, 24–29 July 2000, IRS 2000: CURRENT PROBLEMS IN ATMOSPHERIC RADIATION, edited by: Smith, W. and Timofeyev, Yu., Deepak Publishing, 1140–1143, 2001.
- Martin, R. V., Jacob, D. J., Yantosca, R. M., Chin, M., and Ginoux, P.: Global and regional decreases in tropospheric oxidants from photochemical effects of aerosols, *J. Geophys. Res.*, 108, 4097, doi:10.1029/2002JD002622, 2003.
- Martin, R. V., Jacob, D. J., Chance, K., Kurosu, T. P., Palmer, P., and Evans, M. J.: Global inventory of nitrogen oxide emissions constrained by space-based observations of NO₂ columns, *J. Geophys. Res.*, 108, 4537, doi:10.1029/2003JD003453, 2003.
- Menut, L., Vautard, R., Beekmann, M., and Honoré, C.: Sensitivity of photochemical pollution using the adjoint of a simplified chemistry-transport model, *J. Geophys. Res.*, 105, 15 379–15 402, 2000.
- Middleton, P., Stockwell, W. R., and Carter, W. P.: Aggregation and analysis of volatile organic compound emissions for regional modeling, *Atmos. Environ.*, 24, 1107–1133, 1990.
- Müller, J.-F.: Geographical distribution and seasonal variation of surface emissions and deposition velocities of atmospheric trace gases, *J. Geophys. Res.*, 97, 3787–3804, 1992.
- Müller, J.-F. and Brasseur, G. P.: Sources of upper tropospheric HO_x: a three-dimensional study, *J. Geophys. Res.*, 104, 1705–1715, 1999.
- Müller, J.-F. and Brasseur, G. P.: IMAGES: A three-dimensional chemical transport model of the global troposphere, *J. Geophys. Res.*, 100, 16 445–16 490, 1995.
- Nocedal, J. and Wright, S. J.: *Numerical Optimization*, Springer Series in Operations Research, 1999.
- Novelli, P. C., Masarie, K. A., and Lang, P. M.: Distributions and recent changes in carbon monoxide in the lower troposphere, *J. Geophys. Res.*, 103, 19 015–19 033, 1998.
- Novelli, P. C., Masarie, K. A., Lang, P. M., Hall, B. D., Myers, R. C., and Elkins, J. W.: Reanalysis of tropospheric CO trends: Effects of the 1997–1998 wild fires, *J. Geophys. Res.*, 108, 4464, doi:10.1029/2002JD003031, 2003.
- Olivier, J. G. J., Bouwmann, A. F., Van der Maas, C. W. M., Berdowski, J. J. M., Veldt, C., Bloos, J. P. J., Visschedijk, A. J. H., Zandveld, P. Y. J., and Haverlag, J. L.: Description of EDGAR version 2.0: A set of global emission inventories of greenhouse gases and ozone-depleting substances for all anthropogenic and most natural sources on a per country basis and on 1° × 1° grid, Natl. Inst. of Public Health and the Environ., RIVM, Bilthoven, 1996.
- Olivier, J. G. J. and Berdowski, J. J. M.: Global emissions sources and sinks, in: *The Climate System*, edited by: Berdowski, J., Guicherit, R., and Heij B. J., 33–78, A. A. Balkema Publishers/Swets & Zeitlinger Publishers, Lisse, The Netherlands, ISBN 90-5809-255-0, 2001.
- Olivier, J. G. J., Berdowski, J. J. M., Peters, J. A. H. W., Bakker, J., Visschedijk, A. J. H., and Bloos, J.-P. J.: Applications of EDGAR. Including a description of EDGAR 3.0: reference database with trend data for 1970–1995, RIVM report no. 773301 001/ NOP report no. 410200 051, RIVM, Bilthoven, 2001.
- Olivier, J. G. J.: Part III: Greenhouse gas emissions. 1. Shares and trends in greenhouse gas emissions; 2. Sources and methods: greenhouse gas emissions for 1990 and 1995 in “CO₂ emissions from fuel combustion 1971–2000”, 1–31, International Energy Agency, Paris, ISBN 92-64-09794-5, 2002.
- Olivier, J., Peters, J., Granier, C., Pétron G., Müller, J.-F., and Wallens, S.: Present and future surface emissions of atmospheric compounds, POET Report#2, EU project EVK2-1999-00011, 2003.
- Palmer, P., Jacob, D. J., Jones, D. B. A., Heald, C. L., Yantosca, R. M., and Logan, J. A.: Inverting for emissions of carbon monoxide from Asia using aircraft observations over the western Pacific, *J. Geophys. Res.*, 108(D21), 8828, doi:10.1029/2003JD003397, 2003.
- Peters, J. A. H. W. and Olivier, J. G. J.: EDGAR3/POET Emissions: 1997; Emissions and Scenarios for 1995–2020; Technical Background Information on Global and Regional Sectoral Emissions, Report no. 77330103/2003 (Digital version only), RIVM, Bilthoven, 2003.
- Pétron, G., Granier, C., Khatatov, B., Lamarque, J. F., Yudin, V., Müller J. F., and Gille, J.: Inverse modeling of carbon monoxide surface emissions using climate monitoring and diagnostics laboratory network observations, *J. Geophys. Res.*, 107(D24), 4761, doi:10.1029/2001JD001305, 2002.
- Peylin, P., Bousquet, P., Ciais, P., and Monfray, P.: Differences of CO₂ flux estimates based on a “time-independent” versus a “time-dependent” inversion method, in: *Inverse Methods in Global Biogeochemical Cycles*, Geophysical Monograph, 114, 2000.

- Pickering, K. E., Wang, Y., Tao, W. K., Price, C., and Müller, J.-F.: Vertical distributions of lightning NO_x for use in regional and global chemical transport models, *J. Geophys. Res.*, 103, 31 203–31 216, 1998.
- Price, C., Penner, J., and Prather, M.: NO_x from lightning, 1, Global distribution based on lightning physics, *J. Geophys. Res.*, 102, 5929–5941, 1997.
- Prinn, R. G., Huang, J., Weiss, R. F., Cunnold, D. M., Fraser, P. J., Simmonds, P. G., McCulloch, A., Harth, C., Salameh, P., O'Doherty, S., Wang, R. H. J., Porter, L., and Müller, B. R.: Evidence for substantial variations of atmospheric hydroxyl radicals in the past two decades, *Science*, 292, 1882–1888, 2001.
- Rabier, F. and Courtier, P.: Four-dimensional data assimilation in the presence of baroclinic instability, *Quart. J. Roy. Meteor. Soc.*, 118, 649–672, 1992.
- Richter, A., Burrows, J. P., Nuess, H., Clerbaux, C., Hadji-Lazaro, J., Turquety, S., and Granier, C.: Satellite observations of ozone precursors and ozone, POET Report#1, EU project EVK2-1999-00011, 2003.
- Richter, A. and Burrows, J. P.: Retrieval of Tropospheric NO₂ from GOME measurements, *Adv. Space Res.*, 29(11), 1673–1683, 2002.
- Rodenbeck, C., Houweling, S., Gloor, M., and Heimann, M.: CO₂ flux history 1982–2001 inferred from atmospheric data using a global inversion of atmospheric transport, *Atmos. Chem. Phys.*, 3, 1919–1964, 2003a,
SRef-ID: 1680-7324/acp/2003-3-1919.
- Rodenbeck, C., Houweling, S., Gloor, M., and Heimann, M.: Time-dependent atmospheric CO₂ inversions based on interannually varying tracer transport, *Tellus*, 55B, 488–497, 2003b.
- Rodriguez, M. A. and Dabdub, D.: IMAGES-SCAPE2: A modeling study of size- and chemically resolved aerosol thermodynamics in a global chemical transport model, *J. Geophys. Res.*, 109(D2), D02203, doi:10.1029/2003JD003639, 2004.
- Rossow, W. B., Walker, A. W., Beuschel, D. E., and Roiter, M. D.: International Satellite Cloud Climatology Project (ISCCP) Documentation of New Cloud Datasets, Report WMO/TD-No. 737, World Meteorological Organization, Geneva, 115 pp, 1996.
- Rotman, D. A., Atherton, C. S., Bergmann, D. J., Cameron-Smith, P. J., Chuang, C. C., Connell, P. S., Dignon, J. E., Franz, A., Grant, K. E., Kinnison, D. E., Molenkamp, C. R., Proctor, D. D., and Tannahill, J. R.: IMPACT, the LLNL E-D global atmospheric chemical transport model for the combined troposphere and stratosphere: Model description and analysis of ozone and other trace gases, *J. Geophys. Res.*, 109(D04303), doi:10.1029/2002JD003155, 2004.
- Sander, S. P., Friedl, R. R., DeMore, W. B., Golden, D. M., Kurylo, M. J., Hampson, R. F., Huie, R. E., Moortgat, G. K., Ravishankara, A. R., Kolb, C. E., and Molina, M. J.: Chemical Kinetics and Photochemical Data for Use in Stratospheric Modeling, Evaluation number 13, NASA panel for data evaluation, JPL Publication 00-3, Jet Propulsion Laboratory, Pasadena, 2000.
- Savage, N., Pyle, J., Law, K., Granier, C., Niemeier, U., Clerbaux, C., Hadji-Lazaro, J., Müller, J.-F., Dalsoren, S., Olivier, J., Isaksson, I., Richter, A., Burrows, J., and Wittrock, F.: Intercomparison of chemistry-transport models, POET Report#2, EU project EVK2-1999-00011, 2003.
- Smolarkiewicz, P. K. and Rasch, P. J.: Monotone advection on the sphere: An Eulerian versus semi-Lagrangian approach, *J. Atmos. Sci.*, 48, 793–810, 1991.
- Stamnes, K., Tsay, S., Wiscombe, W. J., and Jayaweera, K.: Numerically stable algorithm for discrete-ordinate-method radiative transfer in multiple scattering and emitting layered media, *Appl. Opt.*, 27, 2502–2509, 1988.
- Streets, D. G., Bond, T. C., Carmichael, G. R., Fernandes, S. D., Fu, Q., He, D., Klimont, Z., Nelson, S. M., Tsai, N. Y., Wang, M. Q., Woo, J.-H., and Yarber, K. F.: An inventory of gaseous and primary aerosol emissions in Asia in the year 2000, *J. Geophys. Res.*, 108(D21), 8809, doi:10.1029/2002JD003093, 2003.
- Talagrand, O.: Bayesian estimation, optimal interpolation, statistical linear estimation, edited by: Swinbank, R., Shutyaev, V., Lahoz, W. A., et al., *Data Assimilation for the Earth System*, 21–35, Kluwer Academic Publishers, 2003.
- Thacker, W. C.: The role of the Hessian matrix in fitting models to measurements, *J. Geophys. Res.*, 94(C5), 6177–6196, 1989.
- Thakur, A. N., Singh, H. B., Mariani, P., Chen, Y., Wang, Y., Jacob, D. J., Brasseur, G. P., Müller, J.-F., and Lawrence, M.: Distribution of reactive nitrogen species in the remote free troposphere: data and model comparisons, *Atmos. Environ.*, 33, 1403–1422, 1999.
- Torres, O., Bhartia, P. K., Herman, J. R., and Ahmad, Z.: Derivation of aerosol properties from satellite measurements of backscattered ultraviolet radiation, Theoretical Basis, *J. Geophys. Res.*, 103, 17 099–17 110, 1998.
- Torres, O., Bhartia, P. K., Herman, J. R., Sinyuk, A., and Holben, B.: A long term record of aerosol optical thickness from TOMS observations and comparison to AERONET measurements, *J. Atmos. Sci.*, 59, 398–413, 2002.
- Tyndall, G. S., Cox, R. A., Granier, C., Lesclaux, R., Moortgat, G. K., Pilling, M. J., Ravishankara, A. R., and Wallington, T. J.: Atmospheric chemistry of small organic peroxy radicals, *J. Geophys. Res.*, 106(D11), 12 157–12 182, 2001.
- Van der Werf, G. R., Randerson, J. T., Collatz, G. J., and Giglio, L.: Carbon emissions from fires in tropical and subtropical ecosystems, *Global Change Biology*, 9, 547–562, 2003.
- Van der Werf, G. R., Randerson, J. T., Collatz, G. J., Giglio, L., Kasibhatla, P. S., Avelino, A., Olsen, S. C., and Kasischke, E. S.: Continental-scale partitioning of fire emissions during the 1997–2001 El Niño/La Niña period, *Science*, 203, 73–76, 2004.
- Wang, Y., Logan, J. A., and Jacob, D. J.: Global simulation of tropospheric O₃-NO_x-hydrocarbon chemistry, 1. Model formulation, *J. Geophys. Res.*, 103, 10 713–10 726, 1998.
- Yienger, J. J. and Levy II, H.: Empirical model of global soil-biogenic NO_x emissions, *J. Geophys. Res.*, 100, 11 447–11 464, 1995.